Optically Stimulated Luminescence from Ag-Doped Lithium Tetraborate ($Li_2B_4O_7$) Crystals

THESIS

Ember S. Maniego, Major, United States Army

AFIT-ENP-MS-16-M-075

DEPARTMENT OF THE AIR FORCE
AIR UNIVERSITY

AIR FORCE INSTITUTE OF TECHNOLOGY

Wright-Patterson Air Force Base, Ohio

AFIT-ENP-MS-16-M-075

OPTICALLY STIMULATED LUMINESCENCE FROM Ag-DOPED LITHIUM TETRABORATE ($Li_2B_4O_7$) CRYSTALS

THESIS

Presented to the Faculty

Department of Engineering Physics

Graduate School of Engineering and Management

Air Force Institute of Technology

Air University

Air Education and Training Command

in Partial Fulfillment of the Requirements for the

Degree of Master of Science

Ember S. Maniego, BS

Major, United States Army

March 2016

AFIT-ENP-MS-16-M-075

OPTICALLY STIMULATED LUMINESCENCE FROM Ag-DOPED LITHIUM TETRABORATE ($Li_2B_4O_7$) CRYSTALS

THESIS

Ember S. Maniego, BS
Major, United States Army

Committee Membership:

Maj Eric M. Golden, PhD
Chair

Dr. Larry E. Halliburton, PhD
Member

Dr. Nancy C. Giles, PhD
Member

AFIT-ENP-MS-16-M-075

Abstract

Silver-doped lithium tetraborate ($Li_2B_4O_7$) crystals emit optically stimulated luminescence (OSL) in response to stimulating light at 400 nm after irradiation with x rays. Photoluminescence, optical absorption, and electron paramagnetic resonance (EPR) were used to identify the defects in the crystal that cause this OSL. Lithium tetraborate crystals have Ag^+ ions at Li^+ sites and at interstitial sites ($Ag_i{}^+$ and $Ag_{Li}{}^+$). Upon ionization at room temperature via x rays, electron-hole pairs are generated. The electrons are trapped at Ag^+ ions which occupy interstitial sites, while the holes are trapped at Ag^+ ions at lithium sites. The trapped electron centers become $Ag_i{}^0$ ($4d^{10}5s^1$) and the trapped hole centers, or recombination centers, become $Ag_{Li}{}^{2+}$ ($4d^9$). Evidence for these centers is seen in EPR spectra taken at room temperature. Optical absorption of the irradiated crystal showed a broad peak near 370 nm. Bleaching with 400 nm light decreased the EPR signals of the $Ag_i{}^0$ and $Ag_{Li}{}^{2+}$ centers. When the crystal was stimulated with 400 nm light, OSL at 270 nm was produced. The OSL intensity decreased as the stimulation wavelength was moved to longer wavelengths away from the 370 nm peak.

The effects of the stimulating light's flux on OSL were observed by using xenon lamp and diode laser sources. OSL, using the more intense laser as the source at 405 nm, decayed faster. It also provided insight on the existence of another competing electron trap, i.e., oxygen vacancies. Their role in the OSL process is explained in this thesis.

OSL with 325 nm stimulation was observed to be higher in intensity by a factor of 2.7 than with 400 nm stimulation. This subject is reserved for future research.

To my beautiful wife and silly son. Thank you for your love and support in this chapter of my life. This is for the Providence that gives us things to study and figure out.

Acknowledgements

I would like to thank my advisor, Maj Eric M. Golden for his willingness to take me as his student when I asked him. He prepared me for my research early by going over concepts and equipment operation months before I was deep into my thesis. He would always go out of his way to help me out, and gave good clear feedback on assignments, papers, and tests. I thank Dr. Larry E. Halliburton for a lot of things. He gave me tips and lessons on how to collect good data, taught me concepts clearly, and got me involved in research work for publication. He taught me the importance of questioning everything, even if it is coming from an expert, and grilled me to make sure I could defend every idea I had. I thank MAJ Brant E. Kananen for his mentorship and his clever suggestions on how to do things better. He was responsible for collecting EPR data referenced in this thesis and helped me with my optical experiments. I thank Mr. Mike Ranft for showing me how to operate the Cary spectrophotometer, and Mr. Greg Smith for showing me how to polish my most precious crystal. Both of them were there for me when equipment issues arose. I thank Dr. Nancy C. Giles for asking me questions that forced me to think deeper about my topic. I thank Dr. John W. McClory for advising me before I started the master's program, and giving me feedback during my research brief to the committee. I thank Mr. Robert Beimler for accepting me into the Army's Nuclear Counter-Proliferation Functional Area and allowing me this opportunity to attend graduate school. I thank my wife for keeping me well-fed and happy, and my son for being my source of joy while in this program.

Ember S. Maniego

Table of Contents

Page

List of Figures

Figure Page

List of Tables

OPTICALLY STIMULATED LUMINESCENCE FROM Ag-DOPED LITHIUM TETRABORATE ($Li_2B_4O_7$) CRYSTALS

I. Introduction

1.1 Background

Lithium tetraborate crystals, abbreviated as LTB, have the chemical formula $Li_2B_4O_7$. It is a uniquely versatile material with many desirable qualities. One of the first studies of LTB in the literature was in the late 1950s when Sastry and Hummel studied the phase diagram of the Li_2O-B_2O_3 system [1]. In this study, only Li_2O-B_2O_3 and Li_2O-$2B_2O_3$ (another way to write LTB) melted congruently at 849 °C and 917 °C, respectively, unlike the other combinations ($2Li_2O$-$5B_2O_3$, Li_2O-$4B_2O_3$, Li_2O-$3B_2O_3$) that melted incongruently. The two that melted congruently meant the composition of the solid and liquid forms were the same. Furthermore, they did not change compositions in their solid temperature ranges. Out of the two, the crystal structure of LTB was studied further by Kroghe-Moe in the following decade, as will be discussed in more detail in Section 1.2 [2, 3].

LTB in crystal form has pyroelectric and piezoelectric properties that make it a suitable material for sensing hydrostatic pressure and heat, and use in robotics [4]. It also has some application in nonlinear optics [5, 6], and surface acoustic wave (SAW) resonators and filters [7]. Boron and lithium nuclei in the crystals have large neutron capture cross-sections which make it a possible neutron detection material [8]. When LTB is doped with transition metals such as copper, silver, and/or manganese, it has potential for radiation dosimetry in the medical field and in defense and security.

The fact that LTB crystals have inherent defects makes it useful in dosimetry. Human tissue has an atomic effective number (Z_{eff}) of 7.42, which is comparable to 7.3 of LTB crystals [9]. This makes it an attractive material for use in personal dosimeters. The defects and the dopants together in the crystal increase the luminescence from the crystal when excited with heat or light. Most of the literature on LTB dosimeters cite the work of Schulman *et al.* in the 1960s as the first research on the topic [10, 11, 12]. According to a secondary source, Schulman experimented on Mn-doped LTB (LTB:Mn), that had thermoluminescence (TL) that emitted at 600 nm, which was insufficient for most photomultiplier tubes [11]. Takenaga *et al.* reported in 1983 that a Cu-doped LTB phosphor had sensitivity to gamma rays 20 times higher than that of Mn-doped LTB [12]. Since that time, LTB:Cu phosphorescent crystals have become a widely used material in medical dosimetry. In recent years, Ag-doped LTB (LTB:Ag) samples were studied for luminescence, as well.

In addition to TL, optically stimulated luminescence (OSL) readout of the LTB crystals has been suggested to be a viable method for dosimetry [10, 13]. Multiple methods of OSL will be discussed later, but in this thesis, the most simple and conventional way of illuminating the material with continuous-wave light is used (known as CW-OSL). The advantage of OSL over TL is the minimization of thermal quenching. Thermal quenching is a decrease in luminescence from a material as heat is applied. McKeever points this out as a "paradoxical" problem because heat is needed to get luminescence [14]. This motivates researchers to look for an alternative dosimeter using OSL.

1.2 Crystal Structure

The lithium tetraborate crystal structure belongs to the space group $I4_1cd$ [2, 3, 15, 16, 17]. It has a tetragonal lattice configuration with a and b axes being equal to

9.475 Å, and the c axis equal to 10.283 Å at room temperature. The crystal has a unit cell made up of 8 formula units of $Li_2B_4O_7$, giving a total of 104 atoms [15, 16, 17]. The building block of the crystal is an anionic unit of $(B_4O_9)^{-6}$ seen in Figure 1.1. The lithium ions distributed in between are ionically bonded to the building blocks, unlike the oxygen and boron ions which are covalently bonded to its neighbors.

Within the $(B_4O_9)^{-6}$ there are subunits of two BO_3 and two BO_4 shared in the unit. They are circled in Figure 1.1 marking the two planar triangles of O1-O2-O3 with B1 in the middle, and two tetrahedra of O1-O2-O3-O4 with B2 in the middle. The planar triangles are not perfect isosceles and the tetrahedra are also not perfect. Their bond lengths listed in Table 1 [17] slightly differ from each other in each subunit.

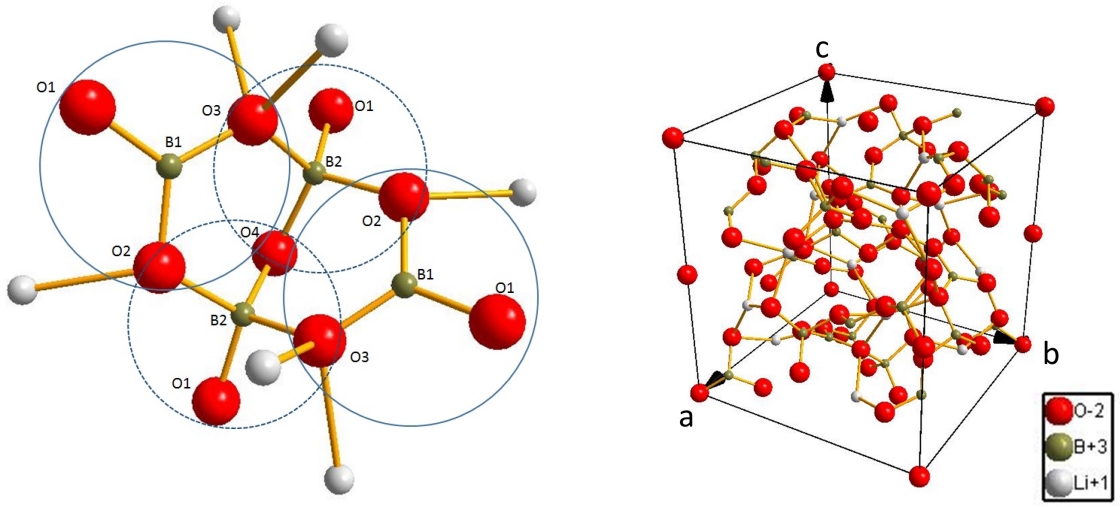

(a) (b)

Figure 1.1. Lithium tetraborate crystal structure. (a) $(B_4O_9)^{-6}$ building block with some lithium ions attached. The solid circles mark the trigonal BO_3 and the dashed circles mark the tetrahedral BO_4. The lithium shown as white spheres are not labeled because they are all equivalent to each other. (b) Unit cell of lithium tetraborate with the basal plane formed by a and b axes, and the vertical cell edges are along the c axis. The diagrams were created using Diamond® software [18].

Table 1. Bond length parameters of BO_3 triangle, BO_4 tetrahedron, and the Li-O_5 polyhedron [17].

Atoms	Bond length (Å)
Planar triangle (B1 center)	
B1-O3	1.370(4)
B1-O1	1.380(4)
B1-O2	1.391(4)
Tetrahedron (B2 center)	
B2-O1	1.427(4)
B2-O4	1.471
B2-O3	1.495(4)
B2-O2	1.512(4)
Polyhedron (Li center)	
Li-aO2	2.013(6)
Li-aO3	2.033(6)
Li-bO3	2.038(6)
Li-aO1	2.206(6)
Li-aO4	2.550

1.3 Motivation and Research Question

There are numerous advantages of OSL over TL. One important advantage is being able to use light as opposed to heat, which may cause damage to the dosimeter material. In addition to that, OSL is much simpler to set up and has less complicated components. It is also much more sensitive than TL. There are few reports of OSL from LTB with different dopants. Rawat *et al.* reported that OSL from LTB:Cu could not be detected; however, the group observed OSL from LTB co-doped with Cu and Ag (LTB:Cu,Ag) [10]. Ratas *et al.* demonstrated that LTB:Mn and LTB:Mn,Be

could be used for OSL readout when they compared data from TL and electron paramagnetic resonance (EPR) spectra [19]. As for the co-doped LTB:Ag,Cu, the main question with this is: could one obtain OSL with just silver impurities? Our preliminary survey of a LTB:Ag crystal showed that OSL emission was possible after the crystal was irradiated with x rays. The question now is: what defects are involved in this particular OSL? This thesis is focused on examining OSL from LTB:Ag, and its relation to photoluminescence (PL) and photoluminescence excitation (PLE), optical absorption, and EPR data. The PL and PLE techniques were used to verify the existence of silver ions. Optical absorption was used to look for wavelengths that could excite or stimulate the LTB:Ag into producing luminescence. EPR was used to determine the defects and their relative concentrations with each other in the crystal.

II. Theoretical Concepts

2.1 Defects

Inorganic crystals such as insulators and semiconductors have defects that give materials desirable or undesirable properties. This thesis is only focused on point defects. One type of point defect is a **vacancy**, which is a lattice site that is missing an intended atom. There is also an **interstitial** which is an atom that is off its intended site in the lattice. An **antisite** is when an atom is on the wrong lattice site in the crystal. These defects are classified as intrinsic. When impurity atoms that are not part of the chemical formula get into the crystal, extrinsic defects are formed. In this case, an external atom may occupy a vacancy site and substitute for the intended atom in that site, or occupy an interstitial site. Defects are introduced in several ways: during the growth process, by heating, by mechanically straining the crystal, by adding ions, or by irradiating [20].

The three ways to look at characterizing a defect are by their geometric, dynamic, and electronic structures [20]. The geometric structure is the shifting of the atoms with respect to the perfect lattice; the dynamic structure looks at the vibrational modes of the atoms; and the electronic structure looks at the electronic states and how defects create energy levels in the band gap of the material. The latter is the most important aspect in this study of LTB:Ag.

2.2 Optically Stimulated Luminescence (OSL)

In the nineteenth century, optically stimulated luminescence was first suggested by Edmond Becquerel, and later, by his son Henri Becquerel when they saw phosphorescence from zinc and calcium sulfide exposed to ionizing radiation [21]. In OSL, light that is used to stimulate a crystal is usually lower in energy (longer wavelength)

and the light emitted is higher in energy (shorter wavelength), given that ionization occurred beforehand. To develop an understanding of this phenomenon and other optical properties, consider the simple energy diagram of a semiconductor shown in Figure 2.1 that breaks OSL up into three stages: (a) excitation, (b) latency, and (c) stimulation [21]. The shaded strip at the bottom of the diagrams represents the valence band with E_v as the upper energy level limit. The valence band is usually completely filled with electrons. The conduction band is represented by the unshaded strip on top of the diagrams with a lower energy level limit at E_c. This energy region is usually empty of electrons, but when an electron is excited into this region, it becomes mobile. There is a forbidden region in semiconductors known as the band gap between E_v and E_c. When energy in the form of particles or radiation, such as γ rays or x rays, is incident on the material, electron-hole pairs are generated (see Figure 2.1a, the excitation stage). This is simply an electron getting excited into the conduction band, leaving a pseudo-particle called a hole in the valence band. When free electrons in the conduction band shift from atom to atom, the holes in the valence band also shift in the opposite direction. If there is an electron in the conduction band, there is a corresponding hole in the valence band, unless there are defects. The net charge of the crystal is neutral so that no charge is gained or lost. The defects in the crystal act as traps for the electrons and holes. Instead of recombining with a hole, an electron may get trapped in a localized energy level about a defect in the

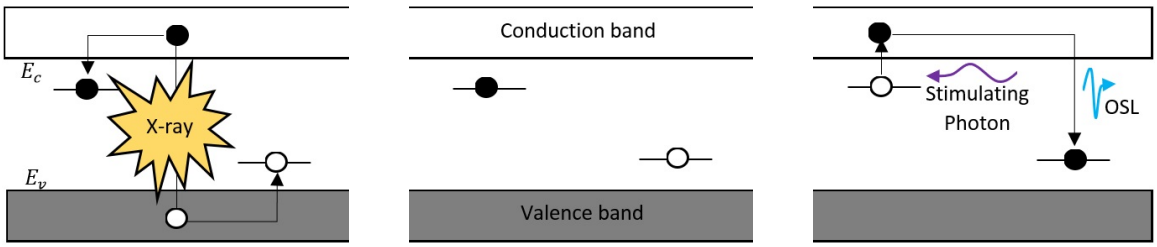

(a) Excitation (b) Latency (c) Stimulation

Figure 2.1. Basic OSL diagram. This figure was adapted from the concept in [21].

gap sometimes referred to as an electron trap. Likewise, the hole may be trapped in a defect in the gap, called a hole trap. In the absence of an ionizing source, the electrons and holes stay in the traps in a metastable state or in the latency stage seen in Figure 2.1b. Depending on the difference between the defect level and E_c, energy in the form of light and/or heat may excite a trapped electron to the conduction band and recombine eventually with a trapped hole. This is illustrated in Figure 2.1c, the stimulation stage, where a trapped electron moves to recombine with the trapped hole to produce OSL. On the other hand, an electron may be excited from the valence band to a trapped hole, creating a hole in the valence band that may move and recombine with a trapped electron in the gap. Both cases bring the material back to its stable state and may emit light as a byproduct.

The model described above is a One Trap One Recombination (OTOR) center model. Chen and Leung used this model in order to solve a system of equations, listed below, that govern the dose dependence of the OSL intensity [22]. Figure 2.2 shows the variables of the OTOR model adapted onto the basic simple OSL scheme. N [m^{-3}] is the concentration of the trapping states (the electron traps in this case), and n [m^{-3}] is the concentration of its occupancy (trapped electrons) with respect to

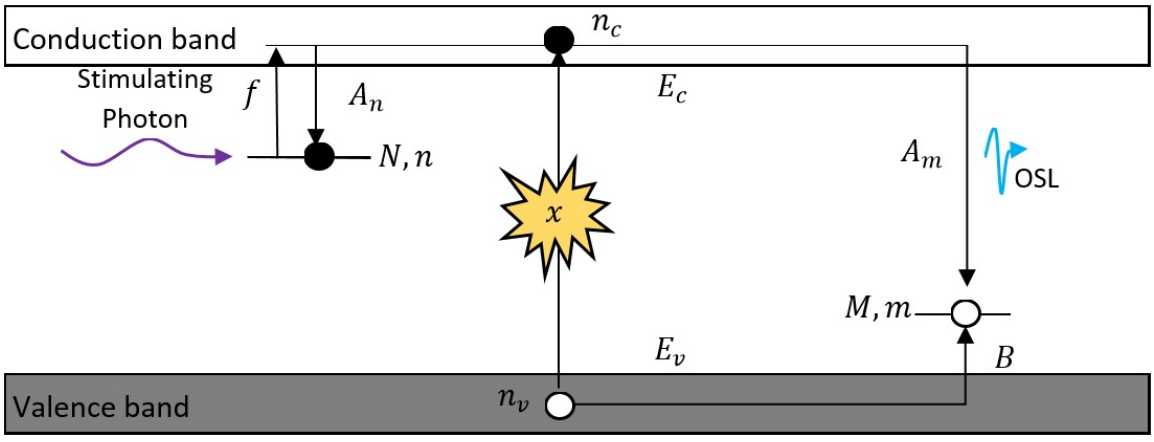

Figure 2.2. One trap one recombination (OTOR) center model of OSL. This concept is from Chen and Leung [22]. See text for reference on the variables and the rate equations for OSL.

time. M [m^{-3}] is the concentration of the recombination centers (hole traps), and m [m^{-3}] is its occupancy (trapped holes) with respect to time (both in m^{-3}). B [m^3s^{-1}] represents the probability coefficient that the holes in the valence band will be trapped in M. Likewise, A_n and A_m represent the probability coefficients that electrons in the conduction band will be trapped at N, and recombine at M, respectively (both in m^3s^{-1}). The concentration of free electrons in the conduction band and the concentration of free holes in the valence band with respect to time are represented by n_c and n_v (both in m^{-3}), respectively. The ionizing radiation intensity is given by x [$m^{-3}s^{-1}$], and f [s^{-1}] (photons per seconds) is the intensity of the stimulating light beam. The rate equations governing the excitation stage are,

$$\frac{dn_v}{dt} = x - B(M-m)n_v, \tag{1}$$

$$\frac{dm}{dt} = -A_m m n_c + B(M-m)n_v, \tag{2}$$

$$\frac{dn}{dt} = A_n(N-n)n_c, \tag{3}$$

$$\frac{dn_c}{dt} = \frac{dm}{dt} + \frac{dn_v}{dt} - \frac{dn}{dt}. \tag{4}$$

The terms $(M-m)$ and $(N-n)$ are the remaining recombination centers and electron traps. When these quantities reach zero, the rate of change of the free holes in the valence band remains constant as long as there is a radiation source ($\frac{dn_v}{dt} = x$). The concentration of recombination centers would decrease as long as there are some free electrons to pull from, but this concentration would be offset as more traps ($M - m \neq 0$) become available to accept more free holes. The concentration of trapped electrons would not increase because the traps are completely filled. The crystal would be at its saturated level for traps, so further irradiation would not be needed.

The rate equations for the stimulation stage are listed below. There is no radiation so $x = 0$.

$$-\frac{dm}{dt} = A_m m n_c = I_{OSL} \quad (5)$$

$$\frac{dn}{dt} = -fn + A_n(N - n)n_c \quad (6)$$

$$\frac{dn_c}{dt} = \frac{dm}{dt} - \frac{dn}{dt} \quad (7)$$

Note that (5) is also the intensity of OSL (I_{OSL}) [$m^{-3}s^{-1}$][1]. Although this thesis is not focused on calculating dose dependence of OSL in LTB:Ag, the variable f is important in the discussion of using different stimulating light sources. The intensity of the lamp source f is proportional to the flux of the stimulating photons ϕ (photons per unit area and time) by the product

$$f\ [s^{-1}] = \sigma\phi, \quad (8)$$

where photoionization cross-section σ is the probability (unit area) that a photon will cause an electron trapped at a defect to move up to the conduction band. This cross-section has a proportionality term, credited to Grimmeiss and Ledebo, that is dependent on photon energy [23]:

$$\sigma(h\nu)\ [cm^2] \propto \frac{(h\nu - E_I)^{3/2}}{h\nu[h\nu + E_I(m_0/m^* - 1)^2]}, \quad (9)$$

where E_I is the energy separation between the defect and the conduction band, and m_0 is the mass of a free electron, and m^* is the effective mass of the electron in the conduction band. When solved numerically, the I_{OSL} with respect to time would look

[1]The unit of OSL intensity here is counts per unit volume per unit time. The spectrofluorometer measures intensity as counts per second (cps).

like an exponential decay, just as a CW-OSL curve; however, it would not be exactly one exponential.

There are many ways to stimulate OSL besides the conventional CW-OSL, which was first proposed by Huntley [24] for archaeological dating. One way is Pulsed OSL (POSL), where the sample is stimulated for less than a second and the emission is collected afterwards. This method is a way to reduce optical filtering requirements and improve radiation sensitivity (i.e luminescence intensity per absorbed dose) [25]. Another way is Delayed OSL (DOSL), where luminescence is measured a few tenths of a second to several seconds after stimulation with light. Setting this time and the wavelength of the stimulating light together, is a way to tune the dosimetry system to different levels of sensitivity [26]. Bulur introduced another technique called linear modulation OSL (LM-OSL) where stimulating light intensity is gradually increased during readout [27]. In this technique, the readout shows peaks instead of decaying curves. All these techniques require more complex setup than the conventional OSL. For this thesis, only CW-OSL is used.

2.3 Thermoluminescence (TL)

In their textbook, Yukihara and McKeever open Chapter 1 with the first written account of thermoluminescence from an experiment by Sir Robert Boyle in which a diamond was held "near the Flame of a Candle, till it was qualify'd to shine pretty well in the dark" [21]. The mechanism for thermoluminescence is similar to that of OSL and can be explained by defects and the energy band model. Instead of light, heat is the stimulating source that releases the electron into the conduction band. One could use the OSL process shown in Figure 2.2 to describe the basic TL process, if the factor f is replaced by $s \cdot exp(-E/kT)$, where E [eV] is the activation energy, s [s^{-1}] is the frequency factor, k is Boltzmann's constant, and T is the temperature.

Knowing E and s is important in determining the thermal stability of OSL [28:143]. Table 2 shows the rate equations and the analogs of each rate in both OSL [22, 28:146] and TL [28:40].

Table 2. Table of rate equations in OSL and TL. (a) System of rate equations during irradiation. (b) System of rate equations during relaxation.

(a)

Rate change in concentration of:	OSL	TL
Free holes	$\frac{dn_v}{dt} = x - B(M-m)n_v$	$\frac{dn_v}{dt} = \frac{dn}{dt} + \frac{dn_c}{dt} - \frac{dm}{dt}$
Recombination centers occupied	$\frac{dm}{dt} = -A_m m n_c + B(M-m)n_v$	$\frac{dm}{dt} = B(M-m)n_v - A_m m n_c$
Trapping states occupied	$\frac{dn}{dt} = A_n(N-n)n_c$	$\frac{dn}{dt} = A_n(N-n)n_c - s \cdot n \cdot exp(\frac{-E}{kT})$
Free electrons	$\frac{dn_c}{dt} = \frac{dm}{dt} + \frac{dn_v}{dt} - \frac{dn}{dt}$	$\frac{dn_c}{dt} = \frac{dm}{dt} + \frac{dn_v}{dt} - \frac{dn}{dt}$

(b)

Rate change in concentration of:	OSL	TL
Recombination centers occupied	$-\frac{dm}{dt} = A_m m n_c = I_{OSL}$	$-\frac{dm}{dt} = A_m m n_c = I_{TL}$
Trapping states occupied	$\frac{dn}{dt} = -fn + A_n(N-n)n_c$	$\frac{dn}{dt} = A_n(N-n)n_c - s \cdot n \cdot exp(\frac{-E}{kT})$
Free free electrons	$\frac{dn_c}{dt} = \frac{dm}{dt} - \frac{dn}{dt}$	$\frac{dn_c}{dt} = \frac{dm}{dt} - \frac{dn}{dt}$

Notice that in Table 2a, $\frac{dn}{dt}$ for TL has the $s \cdot n \cdot exp(\frac{-E}{kT})$ to account for the thermally released electrons at room temperature. This thermal release term is not included for OSL because the trapped electron is assumed to be stable at room temperature.

2.4 Optical Absorption

Different materials have different spectral absorption that is, they absorb certain wavelengths of light and transmit other wavelengths. Some photons are reflected as well. The reflectivity R, absorptivity A, and transmissivity T represent the ratio of the power of light reflected (I_R), absorbed (I_A), and transmitted (I_T), respectively,

over the power of incident light (I_0). When added to together,

$$R + A + T = 1, \text{ and} \tag{10}$$

$$\frac{I_R}{I_0} + \frac{I_A}{I_0} + \frac{I_T}{I_0} = 1. \tag{11}$$

The absorption coefficient is related to the position, z, in the direction of travel of light through the medium by Beer's law,

$$I(z) = I_0 e^{-\alpha z}, \tag{12}$$

where $I(z)$ is the intensity of light at z (unit length) through the medium measured in power over area, α is the absorption coefficient in inverse unit length, and I_0 is the intensity of incident light at $z = 0$. Another term used to quantify the absorbance of a material is optical density (O.D.), which is used by the Cary 5000 spectrophotometer discussed in Section 3.2. This is defined as,

$$O.D = -log_{10}(\frac{I_T}{I_0}), \tag{13}$$

where I_T is the intensity at z [29:4]. The thickness of the crystal is t. Combining with (12), the relationships,

$$O.D. = \frac{\alpha t}{log_e(10)} = 0.434\alpha t, \tag{14}$$

$$\alpha\,[cm^{-1}] = \frac{O.D}{t \cdot log(e)} \tag{15}$$

are derived.

The surface of the crystal affects how photons pass through the material. If the surface is hazy, light incident will scatter in different directions and result in

absorption loss. There is also absorption loss from the reflectivity R, determined from the air-to-material interface equation,

$$R = \left(\frac{n-1}{n+2}\right)^2, \tag{16}$$

where n is the index of refraction dependent on the wavelength λ. Assuming that the multiple reflections inside the crystal are negligible, the transmissivity can be written as [29:4],

$$T = (1-R)^2 e^{-\alpha l}. \tag{17}$$

Substituting this into (13) and rewriting it, the absorption coefficient becomes,

$$\alpha\,[cm^{-1}] = \frac{1}{t \cdot log(e)} \cdot [O.D. + 2log(1-R)]. \tag{18}$$

This is a more complete equation, however, it does not account for scattering losses.

The index of refraction at different λ [nm] can be determined from the Sellmeier equation in the form,

$$n(\lambda)^2 = A_1 + \frac{A_2}{\lambda^2 - A_3^2} + A_4\lambda^2, \tag{19}$$

where A_1,A_2,A_3, andA_4 are coefficients determined to be 2.564310, 0.012337, 0.114467, and -0.019075, respectively, for the ordinary index of refraction of LTB crystals [6]. In this research, only the ordinary index of refraction was used since the crystal was cut so that the electric field vector of the light is perpendicular to the c-axis. Tetragonal crystals are uniaxial with an optical axis along the c-axis. Propagation of light waves along this axis is associated with the normal index of refraction.

2.5 Photoluminescence (PL)

The phenomenon of photoluminescence involves vibronic bands, as well as electronic band theory. The Franck-Condon principle is the rule used to describe the absorption of photons, and the subsequent emission of photons and/or phonons in terms of classical and quantum mechanics. In this rule, there are two different potential energy curves, one for the ground state and one for the excited state of a molecule, or for the purposes of this thesis, a defect. The classical version of the rule is based on very fast electronic transitions, between states, of less than 10^{-15} s, while the vibration, rotation, and translation of the nuclei are "frozen" during the transition [30:328]. This makes the transition vertical on the potential energy diagram, vertical from the initial position, because there is not enough time for the equilibrium position of the excited state to shift. Figure 2.3 shows the configuration coordinate diagram that represents the vibronic levels of a defect in its ground and excited states.

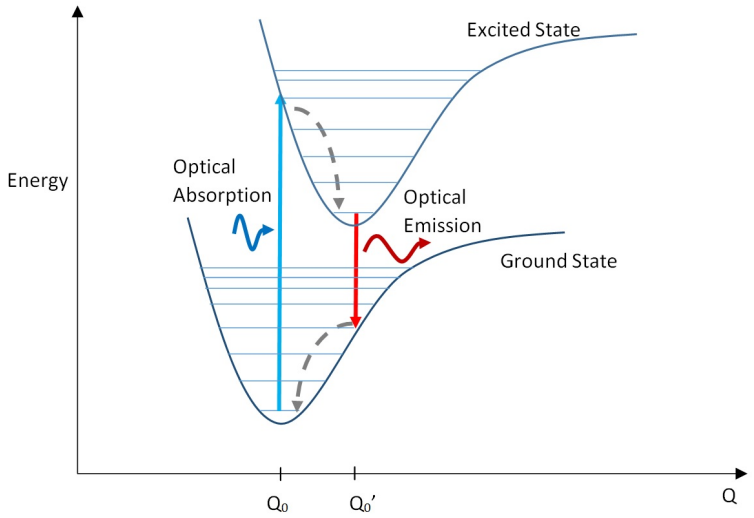

Figure 2.3. This configuration coordinate diagram shows the different potential energy curves of the ground and excited states. The horizontal lines drawn across the potential curves represent the different vibronic levels. The horizontal axis is the generalized coordinate Q and the vertical axis is the energy axis. Q_0 and Q_0' are the equilibrium positions of the ground and excited states, respectively. The optical absorption is shown as a blue arrow, and the emission is shown as red. The gray dashed arrow represents the relaxation by phonon emission to the lowest vibrational energy level in each curve.

The sequence of events in PL starts with the optical absorption to the excited state, followed by the phonon relaxation to the lower vibronic level in the excited state. Conservation of energy dictates emission of a photon upon transition to the ground state curve if the potential curves do not intersect. If potential curves intersect, non-radiative transition between excited and ground state occurs. When the defect is in the ground state, it then relaxes to the lower vibronic level by phonon emission.

Optical transition (by absorption or emission) is determined by the quantum mechanics of harmonic oscillators. The wave function of an electron state i in a vibration level n is written as a product,

$$\Psi_{i,n}(\mathbf{r}, n) = \psi_i(\mathbf{r})\phi_n(Q - Q_0), \tag{20}$$

where $\psi_i(\mathbf{r})$ is the wave function of the electron state with respect to $\mathbf{r}$ — the position vector of the electron— and $\phi_n(Q - Q_0)$ is the harmonic oscillator function in terms of the generalized coordinate Q (in unit length). The Q_0 represents the equilibrium position of the vibration. Fermi's Golden Rule states that the transition rate from one energy level to another is proportional to the square of the matrix element M_{12}. For the transition between excited wave function $\Psi^*_{2,m}$ and ground state $\Psi_{1,n}$, the matrix element is [29:223-24],

$$M_{12} \propto \iint \psi^*_2(\mathbf{r})\phi^*_m(Q - Q'_0)x\psi_1(\mathbf{r})\phi_n(Q - Q_0)d^3\mathbf{r}dQ, \tag{21}$$

or in separate integrals,

$$M_{12} \propto \int \psi^*_2(\mathbf{r})x\psi_1(\mathbf{r})d^3\mathbf{r} \times \int \phi^*_m(Q - Q'_0)\phi_n(Q - Q_0)dQ, \tag{22}$$

where m and n are the vibronic levels of the excited and ground state, respectively.

The first integral term in the product with respect to **r** is assumed to be non-zero, and second integral term is the overlap, or the **Franck-Condon factor**, of the two wave functions . Hence, higher overlap means higher transition probability, and the intensity of light I, absorbed or emitted, is proportional to the Franck-Condon factor by,

$$I \propto \left| \int_0^\infty \phi_m^*(Q - Q_0')\phi_n(Q - Q_0)dQ \right|^2 . \tag{23}$$

One can consider the lengths of blue and red arrows in Figure 2.3, representing the transitions, to be energy [31:209]. Supposing the arrows depicted in the figure are associated with the most overlap or highest Franck-Condon factor, then the rate of photons absorbed or emitted should be the highest at these energies. Away from these energies, the rate of transitions would decrease as shown in Figure 2.4.The difference between peak energies, $E_{absorption}$ and $E_{emission}$ is called the Stokes shift. Specifically, a Stokes shift means a decrease in energy from absorption to emission, and anti-Stokes means the opposite. Stokes shift is involved between PLE and PL. The energy at

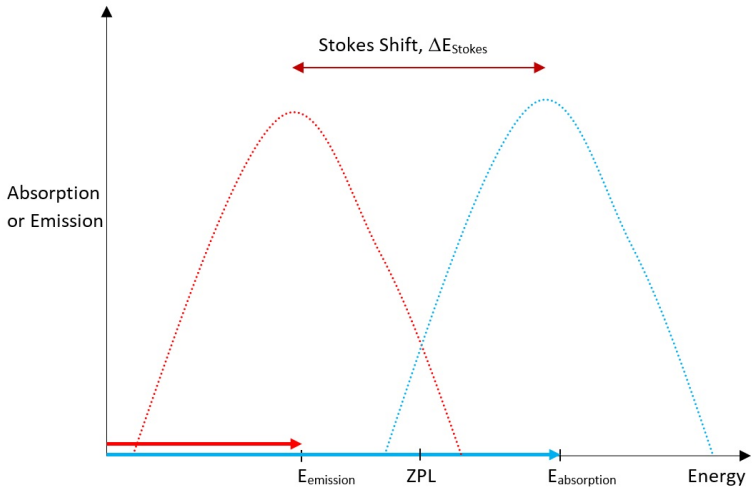

Figure 2.4. Illustration of the Stokes shift with arbitrary band shapes. The transition energy arrows from Figure 2.3 are laid on the energy axis. The $E_{emission}$ is Stokes shifted to lower energy from $E_{absorption}$. ZPL is the zero-phonon line where the transition to and from the excited and ground states occur from the lowest vibronic levels.

which the absorption and the emission bands intersect is the approximate location of the zero-phonon line (ZPL), where optical transition occurs directly between the lowest vibronic levels in both states.

To determine the shape of the absorption band, a dimensionless Huang-Rhys parameter, S, defined as

$$S = \frac{1}{2}\frac{\mu\Omega^2}{\hbar\Omega}(Q_0' - Q_0)^2, \tag{24}$$

where μ is the effective ionic mass and Ω is the vibrational oscillator frequency, is used [29, 31]. The value S is a way to characterize the strength of the electron-lattice coupling between an active ion and the lattice. The Stokes shift can be approximated in two ways by [32]

$$\Delta E_{Stokes} \approx (2S - 1)\hbar\Omega \tag{25}$$

if the potential parabolae were the same [31:208], or

$$\Delta E_{Stokes} \approx 2S\hbar\Omega. \tag{26}$$

The S can be approximated from either of the two equations above if the Stokes shift is known. If the Franck-Condon factor in (23) was considered to be at a temperature of 0 K, so that $n = 0$, the factor is called the zero-temperature Franck-Condon factor, $F_m(0)$. This is related to S by

$$F_m(0) = | < \phi_m^* | \phi_{n=0} > |^2 = \frac{exp(-S)S^m}{m!}, \tag{27}$$

where $\phi_m^* = \phi_m^*(Q - Q_0')$ and $\phi_{n=0} = \phi_{n=0}(Q - Q_0')$. The intensity of the absorption band $I_{ab}(E)$ at 0 K can be written as a series of Dirac delta functions at vibrational modes by

$$I_{ab}(E) = I_0 \sum_m \frac{exp(-S)S^m}{m!}\delta(E_0 + m\hbar\Omega - E), \tag{28}$$

where E_0 is the difference between the bottom of the excited and ground state potential curves ($E^*_{2,m=0} - E_{1,n=0}$), I_0 is the intensity of the full band, and E is the energy of the transition. Likewise, the intensity of the emission band $I_{ba}(E)$ is [31:208],

$$I_{ba}(E) = I_0 \sum_n \frac{exp(-S)S^n}{n!} \delta(E_0 - n\hbar\Omega - E). \tag{29}$$

Figure 2.5 shows the S dependence of the band shape, with the discrete vibronic levels m on the horizontal axis and the $F_m(0)$ value on the vertical axis. If $S = 0$, then this is the ZPL and all the intensity goes to $m = 0$. Furthermore, as S increases, the intensity is distributed to the different vibronic levels in m and eventually starts

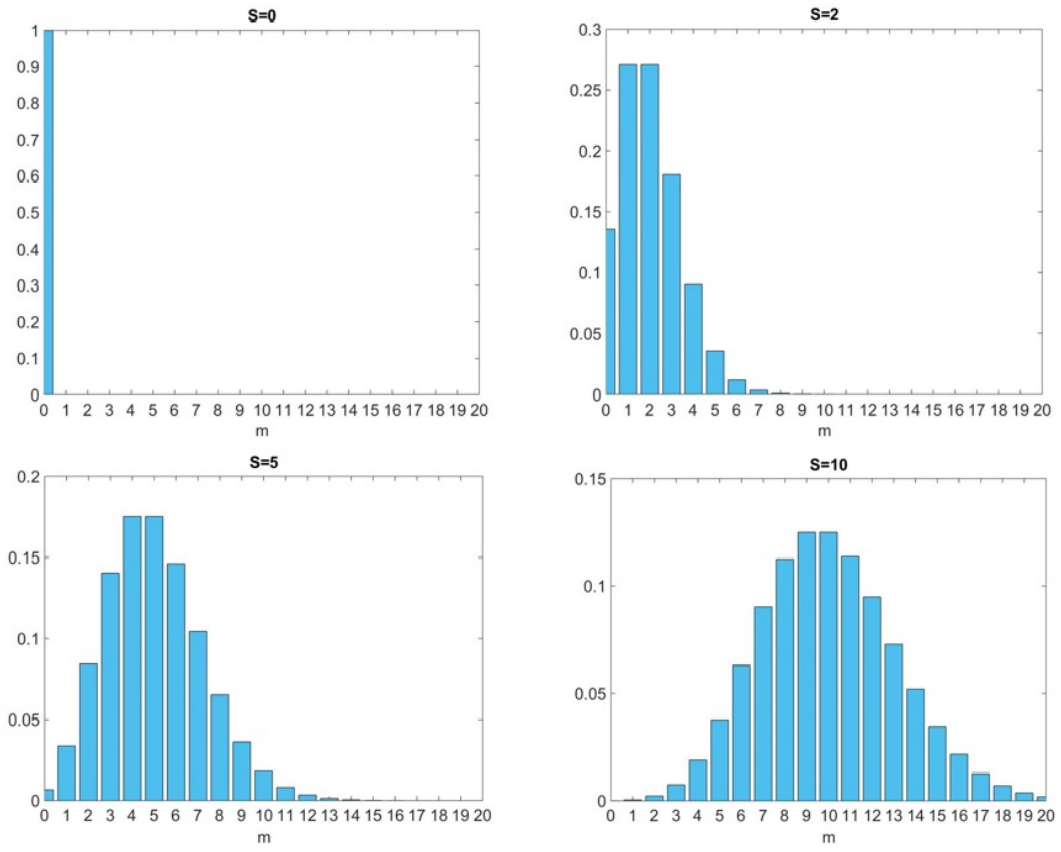

Figure 2.5. This shows the band shape's dependence on the Huang-Rhys parameter, S. The horizontal axis is the vibronic level m and the vertical axis is the Franck-Condon factor at T= 0 K. This assumes $n = 0$ for vibronic level for the ground state.

to look like a Gaussian. Also, the band shape moves farther away from the ZPL as S increases.

2.6 Electron Paramagnetic Resonance (EPR)

Electrons in atoms have intrinsic angular momentum, called spin, that have no analog to classical rotations. These spins are either spin up or spin down ($\frac{1}{2}$ or $-\frac{1}{2}$). Paramagnetism occurs when the magnetic moments of electrons in an atom do not cancel each other. As a result, the atom reacts to an external magnetic field. In electron paramagnetic spectroscopy, much of the electron magnetic dipole comes from the spin angular momentum, and a small part from orbital motion, according to Weil and Bolton [33:7]. In point defects in crystals, electrons or holes distributed over a few atoms lead to paramagnetism that can be detected with EPR.

To understand EPR, consider a simple case of a single electron. The electron has two possible spin magnetic quantum numbers ($m_s = \pm\frac{1}{2}$). Each m_s has magnetic energies U proportional to the magnetic moment μ_z and the magnitude of the magnetic field B, along the z direction, such that $U = -\mu_z B$ [33:20]. Substituting$-g_e\beta_e$ for μ_z gives

$$U = g_e \beta_e B m_s, \tag{30}$$

where $-g_e$ is the free-electron Zeeman factor ($= 2.0023193043617(15)$), and β_e is the Bohr magneton ($= 9.27400949(80) \times 10^{-24}$J T^{-1}). This simple case is illustrated in Figure 2.6, showing the magnetic energy levels splitting apart with increasing magnetic field.

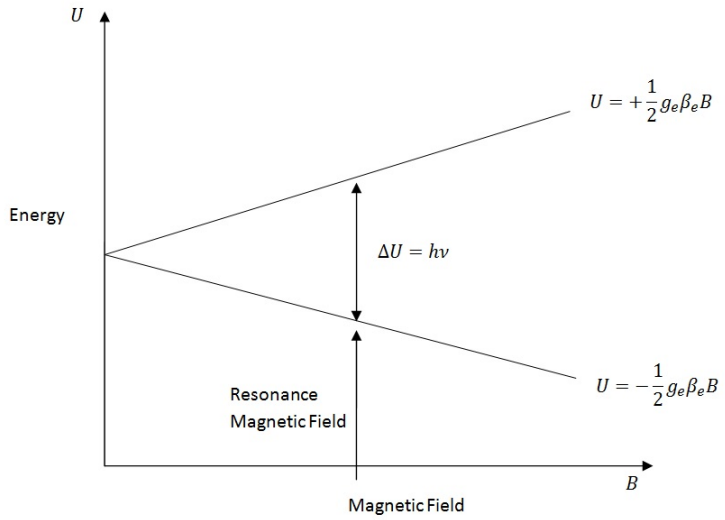

Figure 2.6. Simple electron paramagnetic resonance scheme showing the transition between the lower and upper splitting of magnetic energies at a certain resonant field.

Unlike PL and absorption spectroscopy, where a spectrum is collected over changes in the photon energy, in EPR, the photon energy — in this case the microwave energy — is held constant and the magnetic field is swept across. At a certain field, the microwave energy becomes resonant with the change in the magnetic energies,

$$\Delta U = U_{upper} - U_{lower} = h\nu, \tag{31}$$

where h is Planck's constant and ν is the frequency of the microwaves. There is a transition at this field between the levels as the photon is absorbed.

The actual EPR spectrum is plotted as a first derivative of the absorption of the microwaves from the lower to higher energy. The simple example in Figure 2.7 shows the absorption as a symmetrical peak and the first derivative of it is how the lines in an EPR spectrum appear.

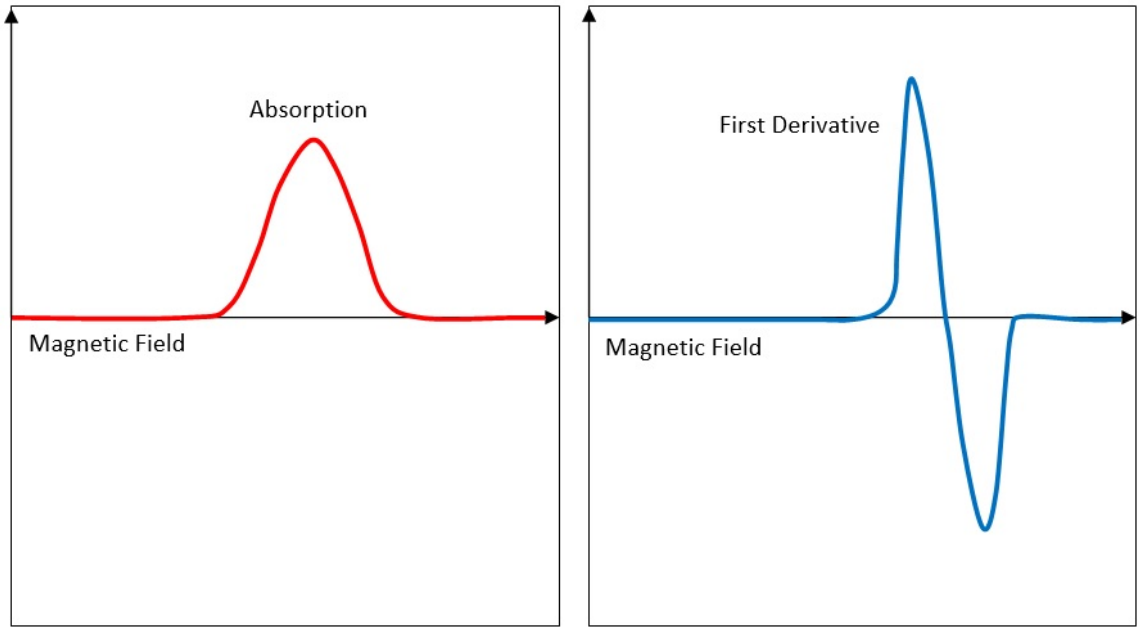

Figure 2.7. EPR absorption and first derivative spectra shapes are shown here. The horizontal axes represent the magnetic field, and the vertical axes represent the signal intensity in arbitrary units.

Beyond the simple case, the g_e factor needs to be replaced by just the plain factor g which is not a single value but a rank 3 tensor. Because of this, EPR spectra will depend on the magnetic field direction. Different materials exhibit different ranges of g [33:24].

Another important EPR concept in this research is the hyperfine interaction between the electron spin and the nuclear spin. The total spin, represented by S, forms a multiplicity of $2S+1$. For example, one unpaired electron with $S = \frac{1}{2}$ has two levels; $S = 1$ has three levels. The nucleus has a total spin I, as well, with multiplicity of $2I + 1$. To illustrate the concept of hyperfine interaction, consider one unpaired electron, $S = \frac{1}{2}$, and a nucleus with a proton and a neutron, $I = 1$. The electron energy level splits into two as seen earlier, and each of these branches is split into three energy levels by the nucleus. Now there are six energy levels and the transition between the levels are constrained by the selection rule that $\Delta m_s = \pm 1$ and $\Delta m_I = 0$. Figure 2.8 shows these three transitions according to the selection rule. The resulting

EPR lines are equidistant from each other by a value called the hyperfine constant a_0.

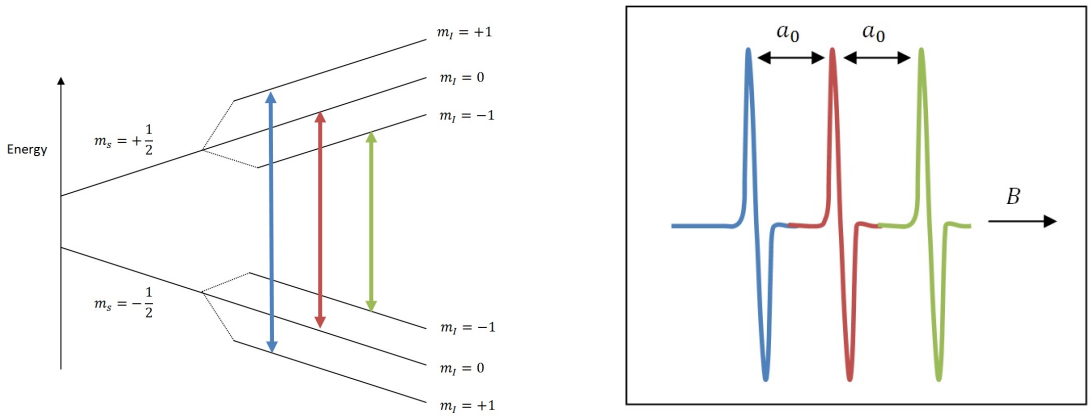

(a) (b)

Figure 2.8. Hyperfine splitting diagram for an $S = \frac{1}{2}$, $I = 1$ system. (a) Shows the hyperfine splitting and allowed transitions based on the selection rule. (b) Shows the resulting EPR spectrum from the hyperfine splitting with equal spacing of a_0.

III. Experiment and Instrumentation

The silver-doped lithium tetraborate crystal used in my experiments was grown using the Czochralski technique at the Institute of Physical Optics in L'viv, Ukraine. It was also the same crystal used in published papers by Brant *et al.* [34, 35]. The Ag concentration was approximately 0.015-0.020 at%. The crystal is rectangular, and its width, length, and depth were measured to be 3.0, 6.6, and 0.84 mm, respectively. The direction along the depth is the c axis of the lattice.

The following sections will explain the data collection procedures used for the experiments and describe the equipment used. The objectives of the experiments were to understand the following:

- PL and PLE of pre-irradiated crystal;
- Optical absorption of pre-irradiated and x-ray irradiated crystal;
- Correlation of optical absorption and EPR spectra upon bleaching with 400 nm light;
- CW-OSL at different stimulation wavelength;
- Spectral dependence of OSL emission; and
- Effects of stimulation photon flux on OSL.

3.1 Irradiation and Annealing

The crystal was irradiated with an industrial x-ray tube manufactured by Varian Medical Systems, enclosed in a wooden box that is lined with lead shielding. The x-ray tube is cooled with water that cycles through a system consisting of a chiller and water filters, and is controlled via a high voltage power supply, Spellman model

FF60P3. During irradiations, the power supply was set to 30 mA and 60 kV for two minutes at room temperature. The current and voltage were gradually raised with control knobs, which I performed in about one minute. I lowered the current and voltage down to 6 mA and 10 kV before shutting off the power supply. This took about one minute also. The maximum current and voltage the x-ray tube can take are 45 mA and 75 kV. One should not raise and lower the current and voltage hastily, because doing so could cause damage. The chosen current and voltage settings were also for precautionary measure to avoid damaging the x-ray tube. Two minutes of irradiation were adequate, and going up to 8 minutes would saturate the electron and hole traps according to previous EPR experiments by B. E. Kananen. As mentioned earlier, the present thesis will not examine dose dependent effects. All we needed was to produce a large concentration of electron-hole pairs.

During irradiation, the crystal was held inside the wall of a paper cup, and in a make-shift "pocket" made with aluminum foil and scotch tape, so that the crystal is aligned with the x-ray tube's exit window about 1 cm away. After irradiation, the induced green color of the crystal gave an indication that the crystal had been irradiated. Care is taken in wrapping the crystal in a small sheet of aluminum foil when transported from instrument to instrument. Ambient light in the laboratory rooms were dimmed while the crystal was mounted on sample holders, to minimize quenching after the irradiation.

To "re-set" the crystal, which means to liberate all holes and electrons from their traps, it was annealed using a Harshaw 3500 thermoluminescence dosimeter (TLD) reader. The crystal was heated to 400 °C at 1 °C/sec and held at the annealing temperature for 180 s. After heating, the crystal was cooled slowly. The lack of color indicated that the traps had been emptied. The crystal was re-set every time before irradiating with x rays to completely empty the shallow traps.

3.2 Optical Absorption Spectroscopy

To collect absorption spectra, I used a Cary 5000 double-beam spectrophotometer, by Varian. It is able to detect absorption of light in the ultraviolet through the infrared (195 to 3300 nm). The spectrophotometer operates by using two beams, as seen in Figure 3.1. The source is either a deuterium (UV) or tungsten-halogen lamp (visible and near infrared). Wavelengths are selected with a rotatable grating in a monochromator. The light is then split into two beams by a chopper which alternately creates a reference beam that passes through an empty sample holder, and a sample beam that passes through the sample. The chopper is a rotating disc with three sections—a transparent window, a mirror, and a blocker. It rotates at 30 Hz according to the Cary 5000 software help menu. When the monochromator beam goes through the transparent window, the beam passes through the sample; at the mirror, the beam goes through the reference; and at the matte black blocker, the monochromator switches to a new wavelength after the chopper has gone through a

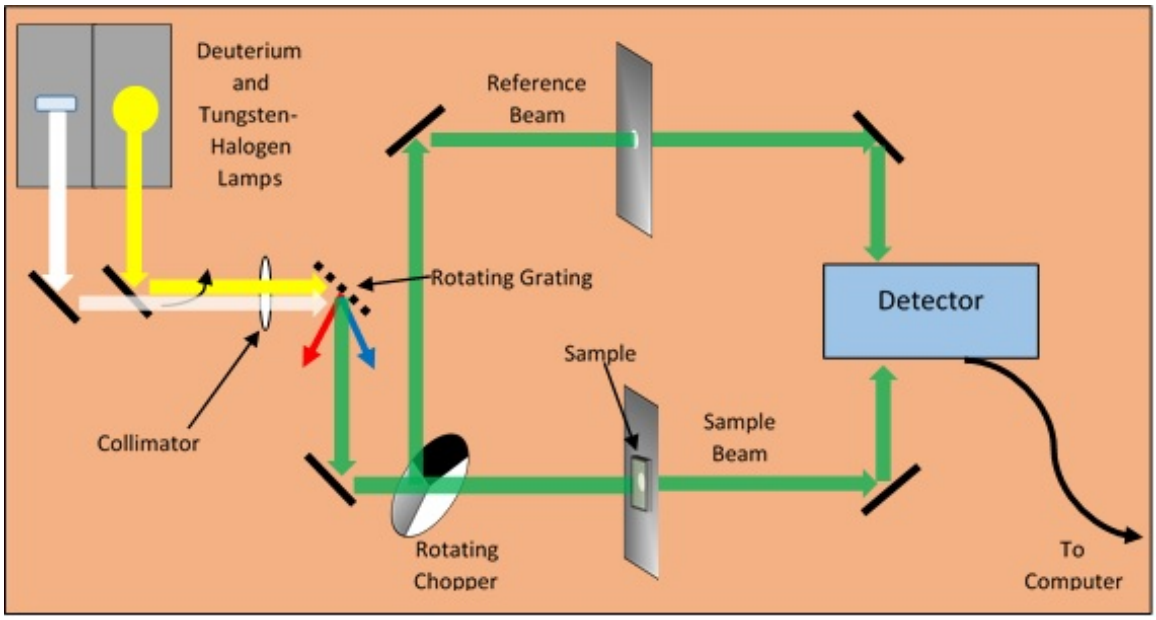

Figure 3.1. Basic diagram of the absorption spectrophotometer (Cary 5000)

number of cycles within the set average time of collection at a wavelength. In all of the absorption experiments, the default average time of 0.1 s was used. The lamp switches to the UV deuterium source at 350 nm after scanning from longer wavelengths with the tungsten-halogen lamps.

For my experiments, the spectrophotometer was set to scan from 800 nm to 195 nm wavelength of light. Baseline correction was performed each time the instrument was used. The sample holders used were two aluminum plates, each with a hole in the middle. The plates did not have a matching aperture size, so the larger of the two was used for the reference beam and the smaller for the sample. In obtaining the baseline correction two scans were conducted by the system for the transmission and absorption. The transmission scan showed approximately less than 100% transmission when the reference plate and the sample plate were placed with nothing blocking the beams. For the absorption scan, the sample beam was obstructed with a mouse pad to ensure 0% transmission. The results of the two scans were used by the computer software in the calculation of the absorption in terms of optical density (O.D). For the real experiments, the crystal was mounted on the sample plate with double-sided clear tape along the sides of the aperture. The crystal covered the whole aperture and was placed in the holder so that the crystal is on the incident side of the plate as pictured in Figure 3.1.

To clear the crystal of surface haze, the LTB:Ag was polished by hand using a metallic puck on which the crystal was glued with Crystal Bond. Using the puck as the holder, the crystal was rubbed on a Buehler polishing pad with a solution of deionized water and a small amount of 1 micron alumina powder. The difference between before and after polishing is shown in Figure 3.2. To correct for reflective losses, equations (16), (18), and (19) were used to correct the data.

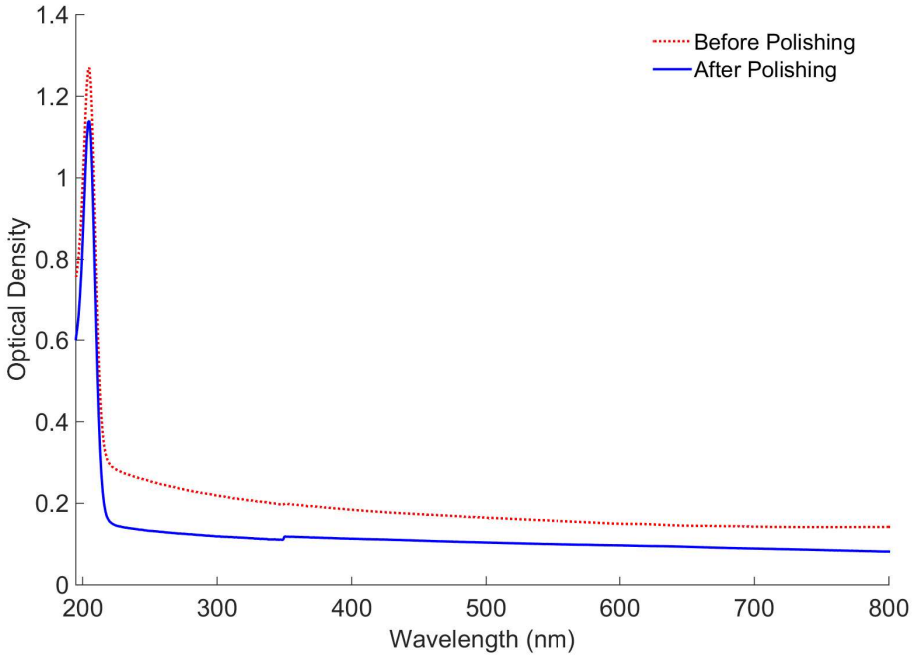

Figure 3.2. Polishing effects on absorption spectrum

3.3 Luminescence Spectroscopy

A spectrofluorometer, controlled via desktop computer, was used to conduct OSL, PL, and PLE studies. The settings parameters in each experiment are described in Chapter IV along with the results. The subsections below describe the procedures and the many considerations to collect reliable data with the system.

3.3.1 Fluorolog Spectrofluorometer

The spectrofluorometer used, made by Horiba Group Jobin Yvon-Spex, is a setup made up of several modules. The one shown in Figure 3.3 is in its FL3-22 model configuration, which is the one used in this thesis.

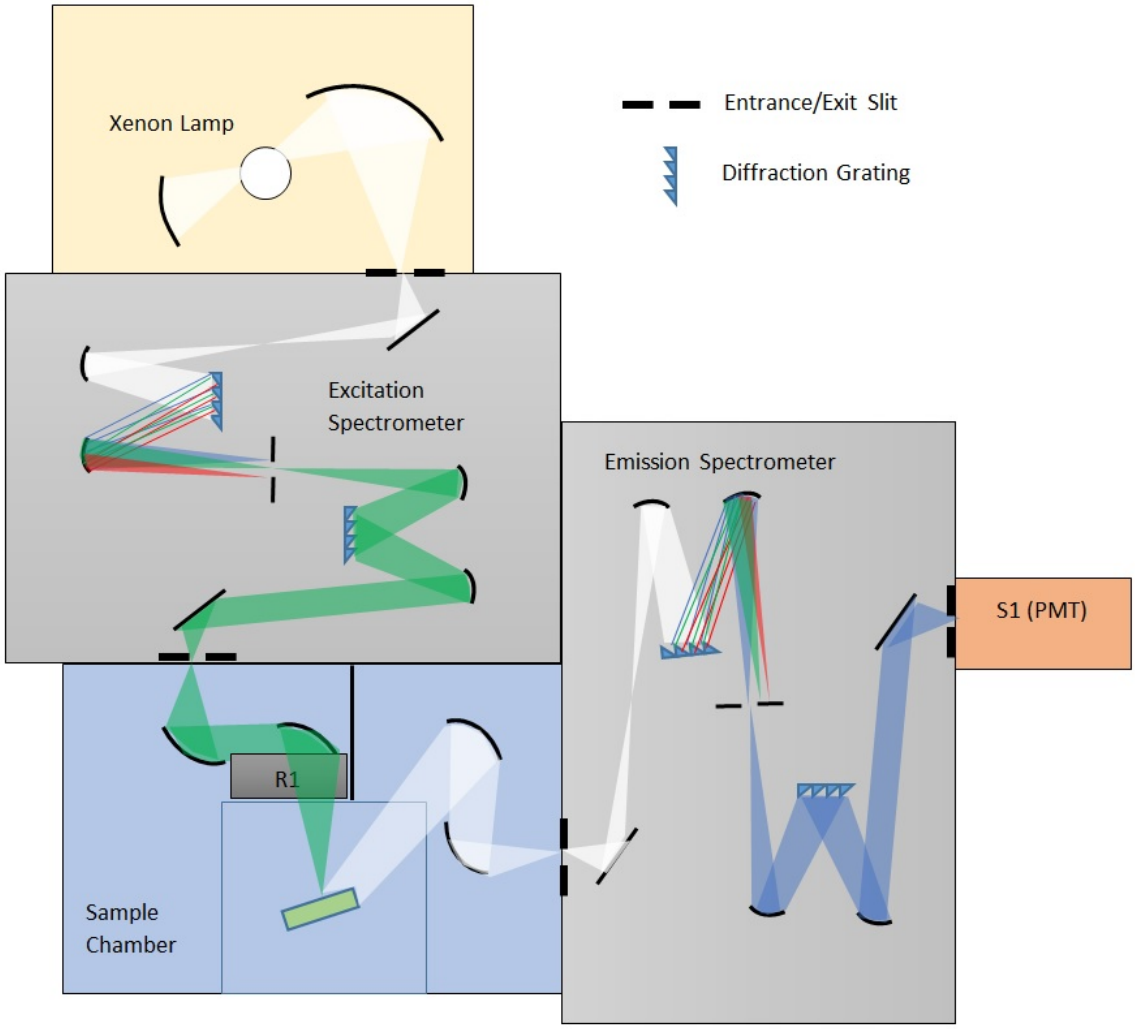

Figure 3.3. Basic diagram of the Fluorolog-3 spectrofluorometer

There is one module consisting of a double grating monochromator and a xenon lamp for exciting the sample, called the excitation spectrometer[1], and one module of the same type for collecting luminescence from the sample, called the emission spectrometer. In the middle is the sample module where the excitation and luminescence are channeled to and from the sample. The monochromators are Czerny-Turner type, which uses reflectors and ruled grating plates that have 1200 grooves per mm. The

[1]The excitation spectrometer and the lamp is also the source of the stimulating light for OSL. The beam coming from this will be referred to as excitation for PL and PLE, or stimulation for OSL.

excitation grating has a 330 nm blaze (200-700 nm range); the emission grating has a 500 nm blaze (300-1000 nm range) [36]. The spectrofluorometer is controlled by a Windows-based computer software package called FluorEssence.

The stimulation or excitation process starts from a 450 W continuous-wave xenon lamp source. This lamp puts out a wide band of light that is collimated onto the reflective diffraction grating, which separates the light into a series of rainbow colors like a prism would. The different colored rays are focused by another mirror onto a plane with a slit. The rotation of the diffraction grating is the method of selecting a narrow band that goes through the slit. Past the slit, the beam goes through another series of collimating mirrors, diffraction grating, and focusing mirror in order to eliminate the stray light (unwanted wavelength of light) that is scattered [36]. The light from the excitation spectrometer is passed through a slit to the sample chamber, and the beam size can be regulated manually by an adjustable aperture. In this research, this aperture is dilated as wide as possible. The light intensity from the excitation spectrometer can be monitored by a diode detector called the reference detector (also referred to as the R1 detector) in units of current (μA).

The luminescence collection process is similar to the above. As with the xenon lamp, the widened band of light coming in from the sample chamber is narrowed down to a specific wavelength to be collected with the R928 photomultiplier tube (PMT) made by Hamamatsu (also will be referred to as the S1 detector). The S1 measures the intensity of luminescence as counts per second (cps) of photons.

In the main experiment menu of the software, there are six types of experiments to choose from. The two main types used in this research are spectra and kinetics. The description of the types of experiment are listed in Table 3.

Table 3. FluorEssence software control settings, experiment types, and parameters for PL, PLE, and OSL experiments. The parameters listed include the values that can be chosen.

Experiment Type	Modes	Spectrum type	Parameters
Spectra	Emission	PL (S1 detector only)	one ex: 200-700 nm Range of em: 300-1000 nm inc: $\geq$ 0.5 nm int time: fraction of a second ex slits (band-pass): 0-15 nm em slits (band-pass): 0-15 nm
	Excitation	PLE (S1 detector only)	Range of ex: 200-700 nm one em: 300-1000 nm inc: $\geq$ 0.5 nm int time: fraction of a second ex slits (band-pass): 0-15 nm ex slits (band-pass): 0-15 nm
	Synchronous	Spectral correction (both R1 and S1)	Range of ex and em: 200-1000 nm inc: $\geq$ 0.5 nm int time: fraction of a second ex slits: 0-15 nm em slits: 0-15 nm
Kinetics	Kinetics	OSL (S1 detector only)	one ex: 200-700 nm one em: 300-1000 nm inc: $\geq$ 0.5 nm int time: fraction of a second ex slits (band-pass): 0-15 nm em slits (band-pass): 0-15 nm time: in seconds

Under spectra, there are three modes: emission, excitation, and synchronous. PL experiments are taken in the emission mode, and PLE experiments are taken in excitation mode. Synchronous mode is used to scan and monitor both excitation light and emission simultaneously (i.e, S1 and R1 detectors are both activated). The kinetics experiment type is only one mode, and this is used for CW-OSL. In this mode, excitation light is set at one wavelength and the emission is set at another wavelength.

The OSL experiment is set to run for a desired length of time. The parameters for the settings, in addition to excitation and emission wavelengths (shortened to ex and em in Table 3), include band-pass slits for both excitation and emission spectrometers (labeled ex slits and em slits), wavelength increments (labeled inc), integration time (labeled int time), and duration (labeled as time for OSL only). The type of detector, either S1 or R1, must be chosen from the set-up window. Multiple consecutive scans can also be selected in these experiments, which is done to obtain the spectral dependence of OSL discussed in Section 4.3.

3.3.2 Calibration of the Spectrofluorometer

The excitation spectrometer was calibrated using the reference detector to ensure that the FluorEssence software accurately measures the wavelengths of light expected from excitation spectrometer with xenon lamp as the source. To do this a scan was conducted from 200 nm to 600 nm. The software was set to scan at 1 nm increments, and the spectrometer slit was 1 nm. The result is shown in Figure 3.4. According to the manual, the double-monochromator has a 467 nm peak at the location labeled [37]. This was then used to make sure it matched the value identified by the software.

The emission spectrometer was calibrated using a pencil-sized mercury argon lamp made by Oriel. The lamp was placed inside the sample chamber and the excitation spectrometer was deactivated so that no light was coming from the xenon lamp. The emission scan was set from 200 nm to 700 nm, at 0.1 nm band pass. The integration time, for increments of 1 nm, was set to 0.5 s for the PMT. The result of the scan in Figure 3.5 is calibrated within 1 nm of the accepted values for the pencil lamp.

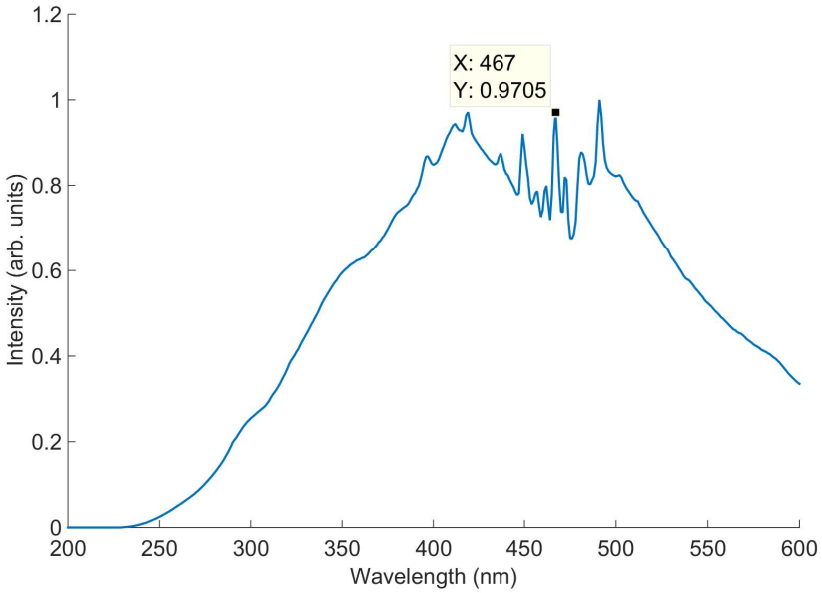

Figure 3.4. Calibration scan of the excitation spectrometer. The peak labeled at 467 nm was used to match the software.

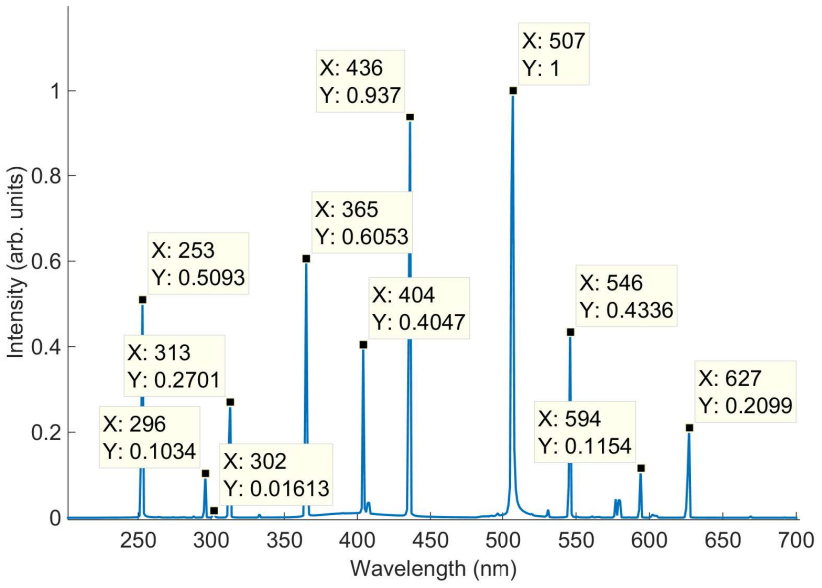

Figure 3.5. Calibration scan of the emission spectrometer. The labeled peaks are within 1 nm of the accepted value. There are some peaks that are second order of another (e.g., 253 nm has second order of 507 nm). Accepted Hg-1 mercury argon lamp spectrum peaks can be found in DeRose [38].

The 1 nm of error is acceptable since the absorption and emission bands of the spectra in this research were much wider than the error. For most of the calibration, these peaks just needed to be verified to be within the acceptance level, and no adjustments were required in the software. Some of the peaks are the result of second order diffraction. From the gratings, orders frequently overlap so a 300 nm wavelength of light passing through a diffraction grating may be detected at 600 nm [39:37]. This is seen, for example, with wavelength pairs 253/507 and 296/594[2].

3.3.3 Corrections

The bands of emitted light, as read by the spectrometer and PMT, are shifted from the actual peaks of these bands. So an attempt to correct for the spectral response was conducted. However, because of the limitation of the Fluorolog spectrofluorometer in the ultraviolet ranges, the correction was inadequate. Information on spectral response correction procedures can be referenced in Appendix A. In lieu of this correction, monitoring emission at the second-order diffraction, suggested by Dr. L. E. Halliburton, was determined to be the best method. It gave optimum signal-to-noise ratio for the PL and PLE experiments, and the results were consistent with previous research (as discussed in Section 4.1). Most of the experiments with the spectrofluorometer were monitored at second-order of emission for this thesis.

When a PL spectrum is converted from wavelength to energy, this process requires correction if the spectrum is taken with a monochromator. This correction is needed because equal energy intervals, ΔE, do not correspond with equal wavelength intervals, $\Delta\lambda$, across a spectrum. This correction method is referred to as the lambda squared (λ^2) correction, and it is more effective with broad energy bands. This correction originates from the Planck's constant and photon energy relationship, $E = h\nu$,

[2]594 nm is the second order diffraction of 297 nm, which is 1 nm within the accepted value of 296.73 nm [38] so it was left as it is.

where the frequency of light ν can be written in terms of the speed of light c and wavelength λ, $E = h\frac{c}{\lambda}$. The change in E with λ is simply the derivative,

$$\frac{dE}{d\lambda} = -\frac{hc}{\lambda^2}. \tag{32}$$

The total intensity across the spectrum is obtained by integrating the intensity $I(\lambda)$ with respect to wavelength,

$$I_{total} = \int_{\lambda_1}^{\lambda_2} I(\lambda) d\lambda.$$

By changing the variables in the integral to make it in terms of E and using the measured intensity $I(\lambda)$ and (32), the total intensity becomes

$$I_{total} = \int_{E_2}^{E_1} I(\lambda) \frac{\lambda^2}{hc} dE.$$

This translates to

$$I(E) = \frac{\lambda^2}{hc} I(\lambda), \tag{33}$$

which is the intensity in terms of energy. However, in this thesis, the product hc will be disregarded since all intensity will be plotted in arbitrary units. Therefore, the raw data from the spectrofluorometer will be only multiplied by λ^2 to get the $I(E)$ curves.

3.3.4 Placement of Crystal in the Sample Chamber

The crystal was stood up on aluminum plates so that it was illuminated by the excitation beam at the center of the chamber where the beam focuses. The location of the crystal was at its optimum location determined from moving the sample around while the excitation lamp was on at 540 nm, and looking at the scattered light from the sample on the entrance slit of the emission spectrometer. For the PL, PLE, and

OSL experiments, the crystal was positioned so that the normal line of one of the broad faces was approximately 20° off the incident excitation beam, away from the direction to the entrance of the emission spectrometer. This was done to minimize the reflection of the excitation beam into the emission spectrometer.

3.3.5 Effects of Stimulation Photon Flux on OSL

The effects of the photon flux of the stimulation beam was observed for OSL. This was done by comparing and constrasting xenon-stimulated and laser-stimulated OSL. The xenon-stimulated OSL was done traditionally with the xenon lamp at 400 nm. The laser-stimulated OSL was done with a 65 mW, diode laser at 405 nm. Preliminary survey of the crystal showed some discontinuities in consecutive OSL runs, with periods of latency in between, for both xenon and laser stimulation. This prompted more thorough experiments of the same type. Without removing the crystal from the sample chamber, OSL runs with the xenon lamp were conducted for 90, 90, and 420 s, totaling 600 s. In between the runs the stimulation light was removed for 6-minute periods. A similar method was conducted for the diode laser, but the lengths of the OSL runs were 30, 60, and 470 s each, totaling 560 s of stimulation. The xenon lamp was deactivated for this laser-stimulated OSL. The laser beam was blocked for the 6 minutes of latency period, while the emission spectrometer detector was kept on. The results from these experiments are discussed in Section 4.3.3.

3.4 Correlation of EPR, Absorption, and Bleaching

To verify the defects involved in the luminescence, absorption scans from the Cary spectrophotometer were compared with the EPR spectra from the Bruker EMX spectrometer. Before the experiment, the crystal was re-set and irradiated. The procedures for the absorption are the same as described in Section 3.2. The bleaching

was done in kinetics mode in the spectrofluorometer with 400 nm light from the xenon lamp, but no OSL spectrum was collected. The following is a list of the sequence of events:

1. Re-set, irradiated, EPR, absorption, bleaching for 50 s;
2. EPR, absorption, bleaching for 50 s (100 s cumulative);
3. EPR, absorption, bleaching for 100 s (200 s cumulative);
4. EPR, absorption, bleaching for 100 s (300 s cumulative);
5. EPR, absorption, bleaching for 200 s (500 s cumulative);
6. EPR, absorption.

The decay in the EPR and absorption scans were compared to determine and associate defects to the OSL.

IV. Results and Analysis

4.1 PL and PLE Results

Prior to obtaining a photoluminescence spectrum, an absorption scan was obtained to verify that the absorption of the pre-irradiated LTB:Ag was at 205 nm as seen in Figure 4.2, in Section 4.2. This was done because in pre-irradiated samples, "Ag^+ ions have an excitation band near 205 nm and emission near 265 nm," according to Brant *et al.* [35]. Kelemen *et al.* reported similar results that assigned emission of 280 nm to the Ag^+ ion also [40]. Parameters for PL and PLE experiments were based on absorption near 205 nm and emission near 265 nm. The purpose of the PL and PLE, is to verify that the crystal studied was consistent with previous reports and that silver ions were present.

The Ag^+ ion with electronic configuration of $4d^{10}$(from $4d^{10}5s$) is non-paramagnetic as all the electrons' magnetic moments cancel each other. EPR would not be able to detect this ion. Ag^+ ion impurities in LTB act as hole traps or electron traps [34]. The ions are hole traps at Li^+ sites ($Ag_{Li}{}^+$), and are electron traps at interstitial sites ($Ag_i{}^+$). When there are no electron-hole pairs, Ag^+ ions absorb 205 nm photons only. Excitation of 210 nm was used to elicit PL, because the excitation spectrometer was inefficient at producing this light at these low wavelengths, so a slightly longer wavelength was chosen. Using the settings in the FluorEssence software listed in Table 3, the result of the PL scan is shown in Figure 4.1. The PL has a peak near 270 nm or 4.6 eV after the corrections in accordance with (33). The peak value of the PL was then used to monitor the PLE plotted in the same figure. The excitation wavelength that emitted the most 270 nm luminescence, was near 208 nm or 5.95 eV. The results here are also consistent with those of Patra and Rawat, who reported 205 nm PLE [10, 41, 42].

Table 4. PL and PLE settings on FluorEssence

Experiment	Settings
PL	ex: 210 nm
	Range of em: 450-650 nm
	inc: 1 nm
	int time: 1 s
	ex slits (band-pass): 10 nm
	em slits (band-pass): 5 nm
PLE	Range of ex: 190-235 nm
	em: 540 nm
	inc: 0.2 nm
	int time: fraction of a second
	ex slits (band-pass): 10 nm
	ex slits (band-pass): 5 nm

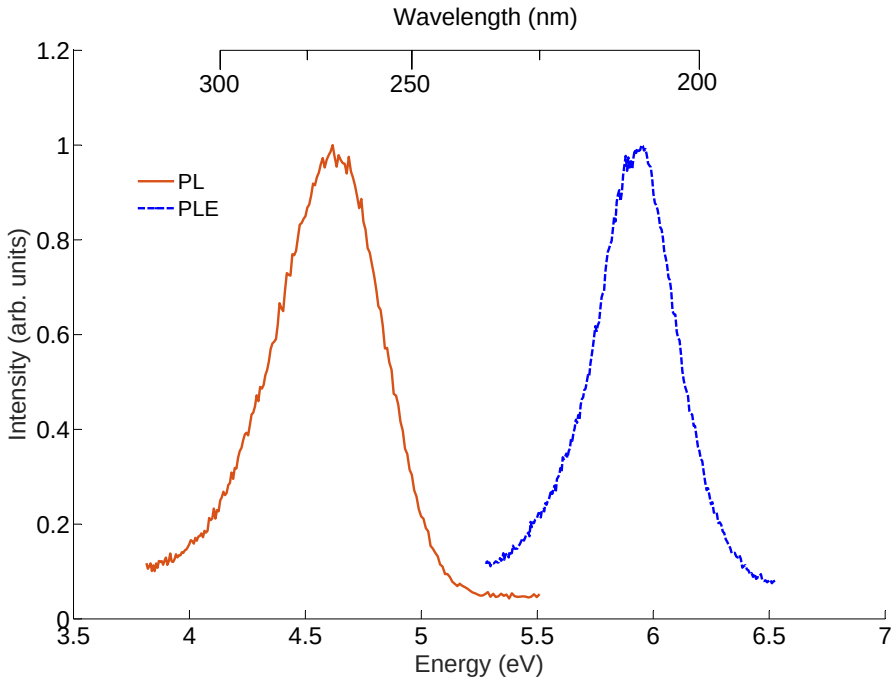

Figure 4.1. PL and PLE data taken with Fluorolog-3

In analyzing the PL and PLE curves, a Stokes shift of about 1.3 eV is observed. The curves do not intersect so there is no access to the ZPL. The full width at half maximum (FWHM) of the PL was 0.54 eV, and 0.41 eV for the PLE. This difference in the width suggests that the potential well curve (see Section 2.5) of the excited state is slightly wider than that of the ground state. In this case, the $4d^{10}$ configuration of the Ag^{+} absorbs the photon and excites to $4d^{9}5s$ configuration, consequently making the wave function more dispersed in the 5s shell and widening the potential well. The transition band from the ground and excited state, representing the PLE, is narrowed as the overlap of the wavefunctions becomes localized to a specific energy of 5.95 eV. From the excited state, the ion relaxes down to the lowest vibronic level emitting phonons, and then goes to its ground state by emitting a photon, since the potential wells do not intersect. Since the ground state potential is narrower, the transition probabilities to other vibronic levels, aside from the most probable one, would be increased. This is why the PL band is wider.

In their studies of Raman scattering of LTB with impurities, Dergachev *et al.* reported an intense line of LTB:Ag at $\bar{\nu}$ =507 cm^{-1}, which corresponds to the polarized vibration at a certain symmetry assigned to the "inclined" optical phonons [43]. The Huang-Rhys factor S can be approximated using (26) with 1.3 eV as the Stokes shift and converting $\bar{\nu}$ to phonon energy in the calculations below.

$$S \approx \frac{\Delta E_{Stokes}}{2\hbar\Omega} = \frac{\Delta E_{Stokes}}{2\bar{\nu}hc}$$

$$= \frac{E_{Stokes}}{2 \times 507\ cm^{-1} \times (4.136 \times 10^{-15} eV\ s) \times (2.998 \times 10^{10} cm/s)}$$

$$= \frac{1.3\ eV}{2 \times 0.0629\ eV} = 10.33$$

The approximate S value of 10 implies that the shape of the PL and PLE are similar to the one shown in Figure 2.5 with $S = 10$. By inspection the shape of the band

predicted from the Huang-Rhys parameter and the data are consistent in that they are both similar to a Gaussian curve.

4.2 Optical Absorption Results

4.2.1 Irradiation vs Pre-irradiation

The raw data from the Cary 5000 spectrophotometer were converted to absorption coefficient, α, and corrected for reflective losses using (16), (19), and (18). The processed optical absorption spectra of the pre-irradiated and x-ray irradiated LTB:Ag is shown in Figure 4.2. The irradiated spectrum showed five peaks near 6.0, 4.8, 4.1, 3.4, and 1.9 eV corresponding to roughly 205, 250, 300, 370, 650 nm, respectively. The absorption band at 205 nm (6.05 eV) is present in both the non-irradiated and irradiated curves. This indicates the presence of Ag^{+} ions mentioned in Section 4.1.

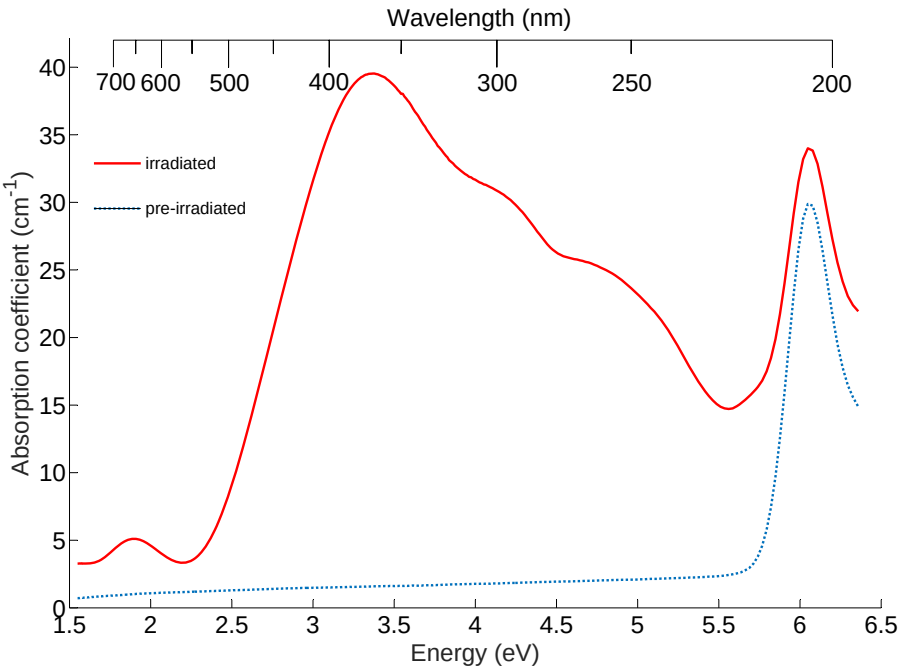

Figure 4.2. Absorption, α, of x-ray irradiated and pre-irradiated LTB:Ag

The green color of the crystal after irradiation agrees with the absorption spectrum having a trough at about 2.2 eV (550 nm), meaning green light is not absorbed but transmitted. In this thesis, the focus is the peak near 370 nm.

Despite the correction for reflective losses, the baseline did not go all the way to zero. The non-irradiated spectrum still shows an incline towards 6.0 eV where no absorption is expected. This increase in absorption can be explained by Rayleigh scattering (light scattered is proportional to $1/\lambda^4$). As the spectrophotometer scans from wavelengths 800 to 195 nm, the computer processes light lost from scattering as absorption. This scattering loss is higher at shorter wavelengths (higher energy) which explains the gradual increase of the baseline.

The major feature of the absorption spectrum near 370 nm is assigned to the electron trap defect. Brant *et al.* reported that x-ray irradiation of LTB:Ag produces equal concentrations of Ag_i^0 and Ag_{Li}^{2+} as seen from EPR techniques [35]. It follows from the fact that the number of electrons and holes produced during ionization must be equal. In that same paper, the researchers tentatively assigned the 370 nm absorption band to the transition from $4d^{10}5s^1$ to $4d^{10}5p^1$ of Ag_i^0 (neutral silver). This assignment was based on high resolution spectroscopy of neutral silver that showed absorption at 338 nm ($^2S_{1/2}$ to $^2P_{1/2}$) and 328 nm ($^2S_{1/2}$ to $^2P_{3/2}$) during the 5s to 5p transition in the gas phase [44]. Furthermore, Sousa *et al.* reported that the $4d^{10}5p^1$ state of silver in Ag-doped KCl crystals has a delocalized electron that reaches the conduction band, after an absorption of 425 nm light [45]. Thus, for this thesis, Ag_i^0 is assigned as an electron trap that absorbs photons near 370 nm. The peak near 297 nm can be seen in the absorption spectra and has been reported in literature to emit 502 nm and 702 nm of luminescence [35, 46], after x-ray irradiation at room temperature. From EPR correlation experiments in the past, the emissions at 502 nm and 702 nm were assigned to the two Ag_{Li}^{2+} hole trap centers— the 502

nm is associated with the hole center isolated from a nearby defect, and the 725 nm with the hole center with a nearby perturbing defect [35]. These two hole trap centers are discussed later in this section.

The 205 nm peak of the irradiated crystal showed higher absorption coefficient than that of the pre-irradiated crystal. This could lead to the wrong interpretation that there were more Ag^+ ions in the irradiated crystal. However, this was not the case since some of those Ag^+ ions were converted to Ag_i^0 and Ag_{Li}^{2+} after x-rays. The concentration of absorbing defects is proportional to the O.D., and by (14), is also proportional to α. However, the α of the 205 nm peak is compounded with those of the broad bands from 2.5 eV to 5.5 eV, for the irradiated case. To obtain a better estimation of the relative concentrations, the difference of the α values at the peak at 205 nm and that of the base at 220 nm were taken. For the irradiated crystal, this difference was 19 cm^{-1}, and the pre-irradiated had 28 cm^{-1}. This meant that there were relatively more Ag^+ ions in the pre-irradiated condition.

4.2.2 Correlation of Optical Absorption, EPR, and Bleaching

The absorption decayed as the irradiated crystal was bleached with 400 nm light from the xenon lamp, using the experimental procedures in Section 3.4. Figure 4.3 shows the series of optical absorption scans immediately after the irradiation, and cumulative bleaching times thereafter. The curves of the absorption spectrum decreased, as expected, since the metastable Ag_i^0 traps were stimulated to free their electrons. The freed electrons recombined with Ag_{Li}^{2+} ions to make Ag_{Li}^{+} ions. To determine the relative concentration of the traps, the differences between the peak and the base were taken. For the Ag_i^0 electron traps associated with the 370 nm peak, the absorption coefficient value at 564 nm (trough) was subtracted from that

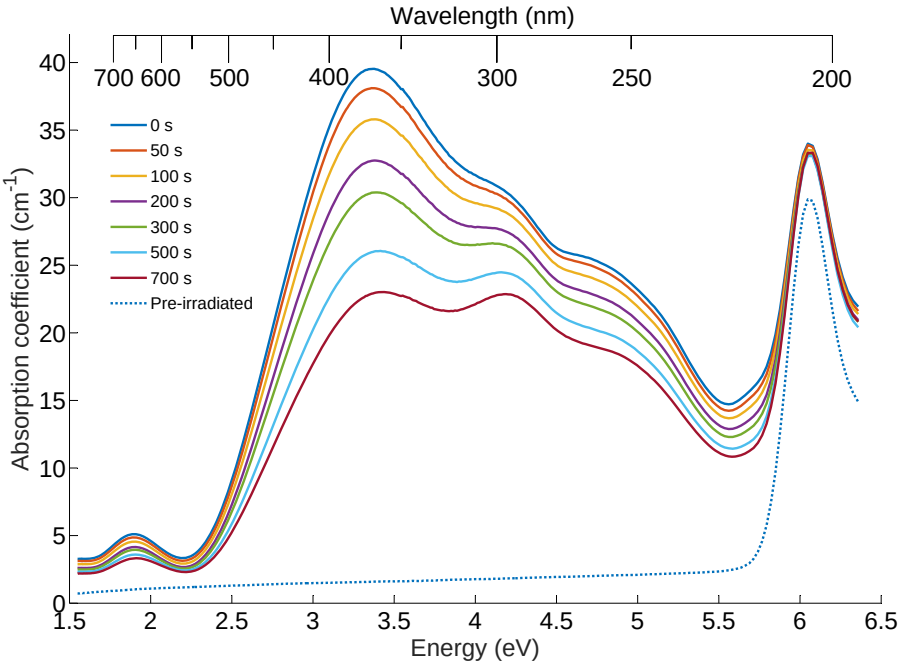

Figure 4.3. Absorption decay with cumulative bleaching times after x-ray irradiation. The pre-irradiated spectrum is included.

at 368 nm[1] from each of the optical absorption curves at different times. For Ag^+ associated with the 205 nm peak, absorption values at 205 nm and 220 nm were subtracted. These differences are plotted in Figure 4.4. The fitted lines show that there is a decrease in the peak-to-base difference with respect to the bleaching times for the 370 nm (3.4 eV) peak, and an increase for the 205 nm (6.05 eV) peak. This implies that the relative concentration of Ag_i^0 decreased with 400 nm bleaching as the electrons from Ag_i^0 went to the Ag_{Li}^{2+} to become Ag_{Li}^+. The relative rates of increase and decrease do not balance out, because the 370 nm peak is also compounded with the bands at shorter wavelengths. The disparity may also be partly attributed to other electron traps that prevent free electrons from recombining with Ag_{Li}^{2+} to form more Ag_{Li}^+ ions. One such competing trap detected with EPR by B. E. Kananen are

[1]Absorption at 368 nm had the highest value so it was chosen for the maximum instead of 370 nm.

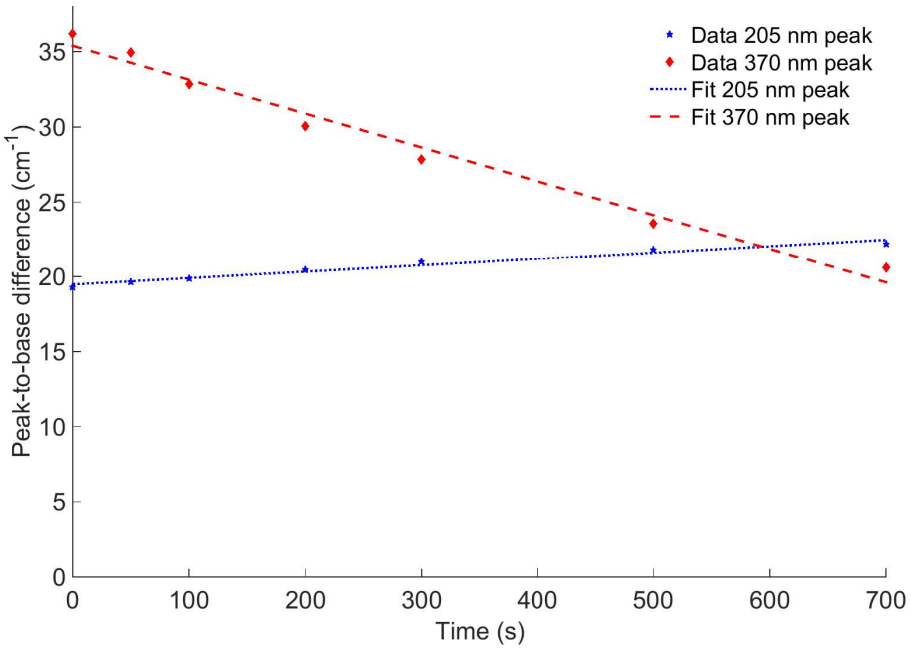

Figure 4.4. Plot of the peak-to-base difference of the 370 nm and 205 nm peaks of absorption at the cumulative bleaching times.

oxygen vacancies, discussed later in Section 4.3.

A series of EPR spectra taken along with each of the absorption spectra in Figure 4.3 provides insight on the defects involved in luminescence. Figure 4.5 shows the spectra immediately after irradiation, and 700 s after bleaching with a xenon lamp. There were five other spectra, not shown in the figure for the 50 through 500 s bleaching times, that showed the electron traps decreased. The signal of the electron traps are made up of the 16 lines centered at 333.0 mT. According to research in the past, the EPR data show hyperfine interactions with ^{109}Ag and ^{107}Ag, and with a neighboring $I = \frac{3}{2}$ nucleus for the Ag_i^0 electron traps [34, 46]. In previous research with Cu-doped LTB, the hyperfine lines of the electron trapped at Cu^0 were reported to be caused by ^{11}B that has an $I = \frac{3}{2}$ nuclear spin and 80.1% abundance, as opposed to ^{10}B with $I = 3$ and 19.9% abundance [47]. Therefore, the 16 lines were assigned

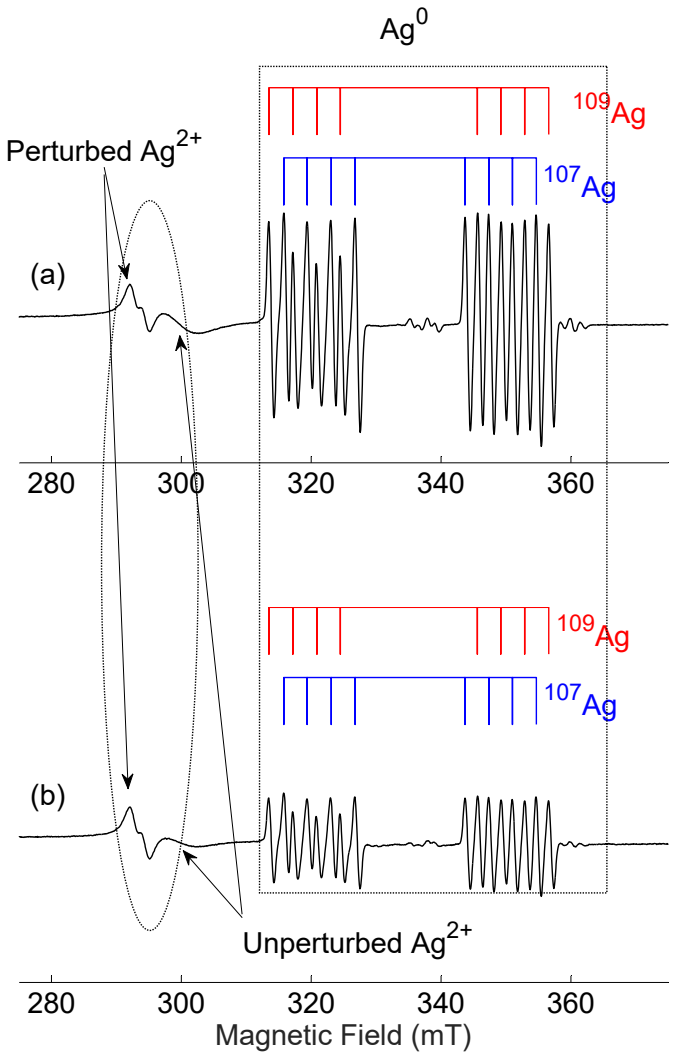

Figure 4.5. EPR data showing the defects involved in bleaching the irradiated LTB:Ag. The red and blue lines indicate the hyperfine interactions of ^{109}Ag and ^{107}Ag and with a neighboring $I = 3/2$ nucleus [34]. The dashed ellipse marks the hole traps, and the dashed rectangle marks the electron traps. The figures shown were processed from the spectra taken at room temperature by B.E. Kananen. Spectrum (a) is the EPR data right after x-ray irradiation, and (b) is the data after 700 s of bleaching at 400 nm with the xenon lamp.

to ^{11}B interactions in this thesis. This further proves that the electron traps are Ag^+ ions occupying interstitial positions (hence the notation Ag_i^+) in the crystal near boron sites. If Ag^0 atoms were in Li sites, then the B^{3+} would be too far away from

it to have intense hyperfine lines (2.7478 Å [18] is the minimum Li-B distance). The sizes of the Ag^+ and Li^+ ions also suggest that during the growth of the crystal, the Ag^+ ions would be more likely to occupy interstitial sites because they have a larger radius than the Li^+ ions (1.15 Å for Ag^+ and 0.76 Å for Li^+).

On the lower magnetic field end of Figure 4.5, the unresolved lines from 290 to 300 mT show the two hole traps. Under low temperatures, these spectra are two intense and highly resolved doublets seen in Figure 4.6. One doublet with the two higher intensity lines is assigned to the unperturbed Ag_{Li}^{2+}. The other doublet with the lower intensity lines is the perturbed Ag_{Li}^{2+}. The reader is referred to the papers by Brant [34] and Buchanan [46] for more information on these. Basically, the four lines representing both perturbed and unperturbed centers are due to the hyperfine interaction of the electron spin with the nuclear spin of the Ag_{Li}^{2+} ions ($I = \frac{1}{2}$).

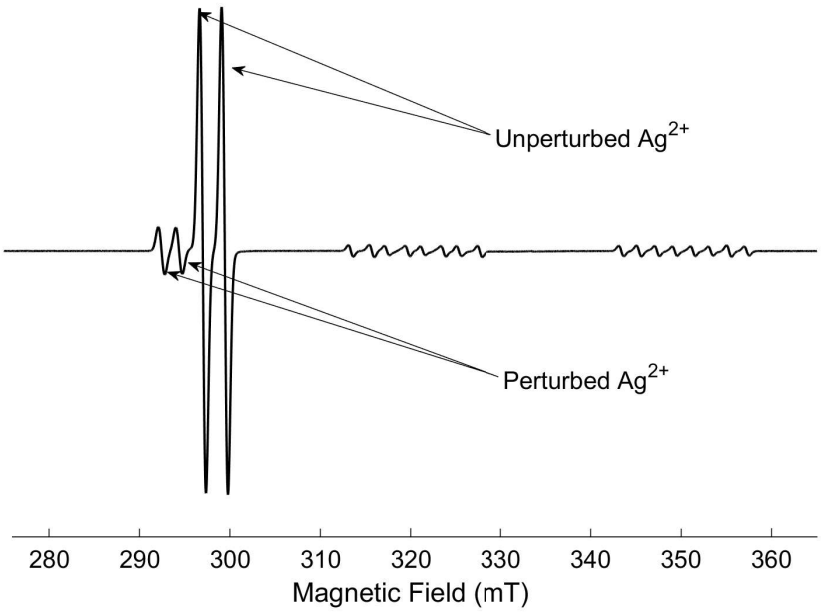

Figure 4.6. EPR spectrum of hole traps at low temperature. The data show the doublets of the perturbed and unperturbed hole traps of x-ray irradiated LTB:Ag, taken at 30 K.

According to selection rules mentioned in Section 2.6, there would be two energy transitions from this hyperfine interaction for each center. At room temperature, these lines broaden, shrink and overlap with each other creating a wavy pattern that does not resemble the resolved lines in Figure 4.6. However, at room temperature, the right part of the unperturbed center's signal does not overlap with the perturbed signal, and can be seen as a dip slightly to the right of 300 mT in Figure 4.5. As the irradiated crystal was bleached, the dip representing the unperturbed traps decreased in magnitude, showing that these hole trap centers were the recombination centers of the electrons released from the Ag_i^0 traps. The perturbed traps did not seem to have decreased, which means the electrons were more inclined to recombine with holes that were isolated from other defects.

The relative concentration of the defects can be obtained from EPR data by measuring the height of a single line from top to bottom. B. E. Kananen took the first line of the electron traps from each EPR spectrum to determine the relative concentrations of electron traps (Ag_i^0) at the 0, 50, 100, 200, 300, 500, 700 s cumulative bleaching times. Relative concentrations of the holes were determined from taking the difference between the dip of the spectrum in Figure 4.5 and the baseline, and multiplying the difference by 2. These were compared with the relative concentration of the electron traps using absorption data in Figure 4.3. Unlike before, the α value of the pre-irradiated curve at 368 nm (1.59 cm^{-1}) was used as the baseline and subtracted from the 368 nm absorption coefficients of the x-ray irradiated curves at the different bleaching times. The plots of these were normalized and combined together in Figure 4.7, which shows close correlation, but not exact. This is probably due to the fact that in EPR, the entire concentrations of specific defects are accounted for, and the defects could be distinguished from one another. Whereas, with the absorption, the broad absorption band at 370 nm has a mixture of other absorption bands. The band

centered around 370 nm can be fitted with two Gaussian curves. There were also other underlying bands like those near 650 nm and on the shorter wavelength side of the 370 nm peak that have peaks associated with them (297 nm and 325 nm). By careful inspection of Figure 4.3, one may see that the 370 nm peak shifts slightly towards a shorter wavelength as the crystal is bleached, suggesting that there is an underlying peak at higher energy. These peaks are convolved so the relative concentrations are over-estimated. Regardless of the reason, the correlation suggests that the 400 nm bleaching light caused the electrons at the Ag_i^0 traps to excite into the conduction band, and recombine with the trapped holes at the Ag_{Li}^{2+}. The results here support the results from the OSL experiments in the next section.

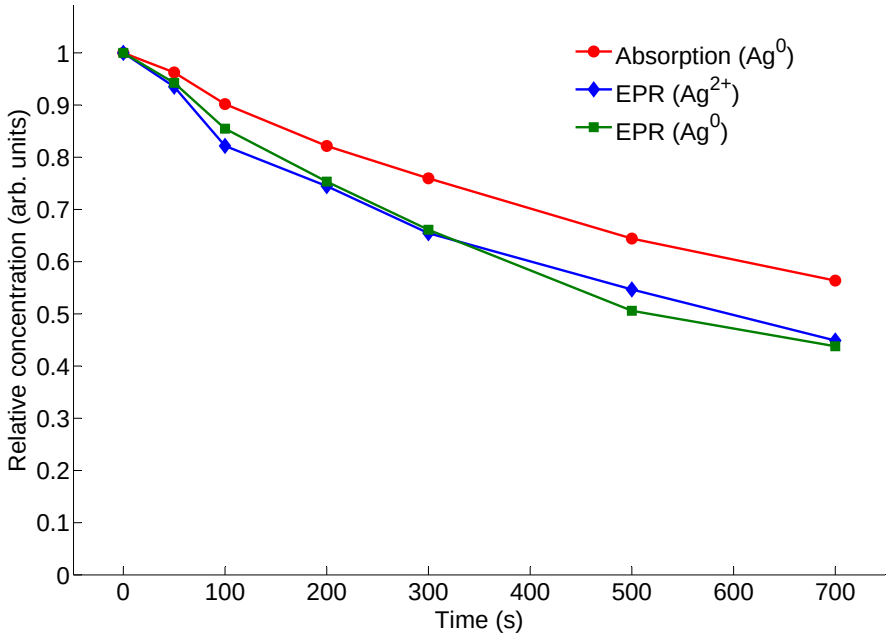

Figure 4.7. This figure shows the correlation of the relative concentrations of the Ag_i^0 electron traps and the Ag_{Li}^{2+} hole traps determined from the optical absorption data and EPR data.

4.3 OSL results

4.3.1 OSL at Different Excitation Energies

A series of OSL spectra were taken following the procedures outlined in Section 3.3 to see the effects of stimulating light at different wavelengths. Each scan was stimulated at 400, 450, 500, and 650 nm, but the following setting parameters were kept the same in each scan:

- excitation and emission slits were 10 and 5 nm, respectively;
- emission monitored at second order of 270 nm (540 nm);
- and integration time was 0.5 s.

The crystal was re-set and x-ray irradiated for 2 minutes each time with procedures

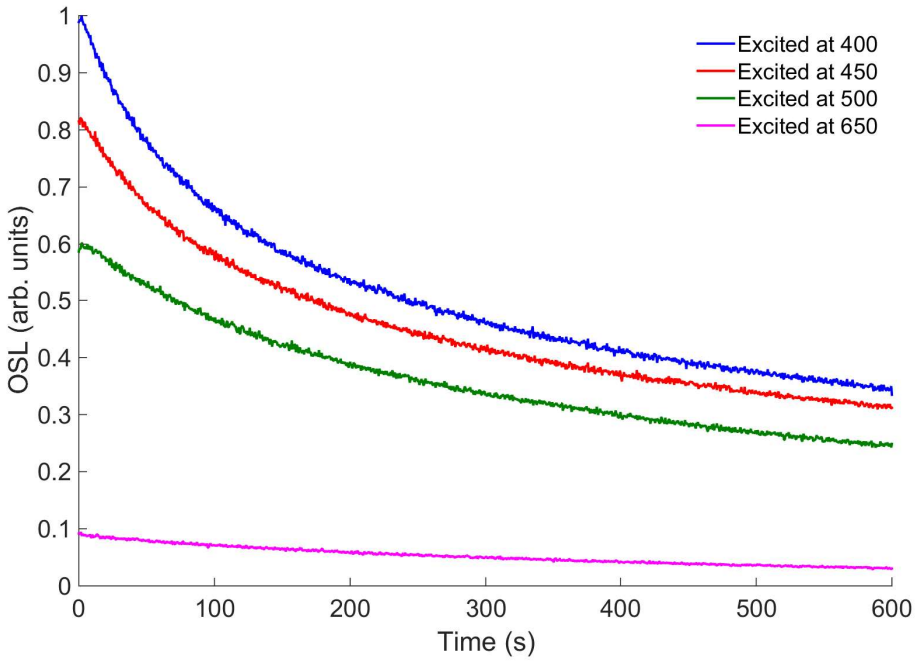

Figure 4.8. OSL at different excitation wavelengths. The order of OSL curves from top to bottom correspond to the the increasing wavelengths of excitation light.

from Section 3.1. The wavelength dependent plots of the OSL are shown in Figure 4.8.The curves look exponential but are not exactly exponential as mentioned before. There are fast and slow components in the curves, and oxygen vacancies may be partly responsible for this slow component.

There is a correlation between the decrease in the initial OSL intensity and the x-ray irradiated absorption data in Figure 4.2. For the absorption data, the difference between the absorption coefficients at each of the excitation wavelengths and at the trough around 564 nm (2.2 eV), were taken and normalized. For the OSL, the initial intensities at 0 s were taken and normalized to the initial intensity of OSL when stimulated with 400 nm light. Figure 4.9 shows the decrease in both absorption and OSL, but the plots do not exactly align. The absorption seems to decrease faster than the OSL from 400 to 500 nm. The difference in how the rates go down is simply

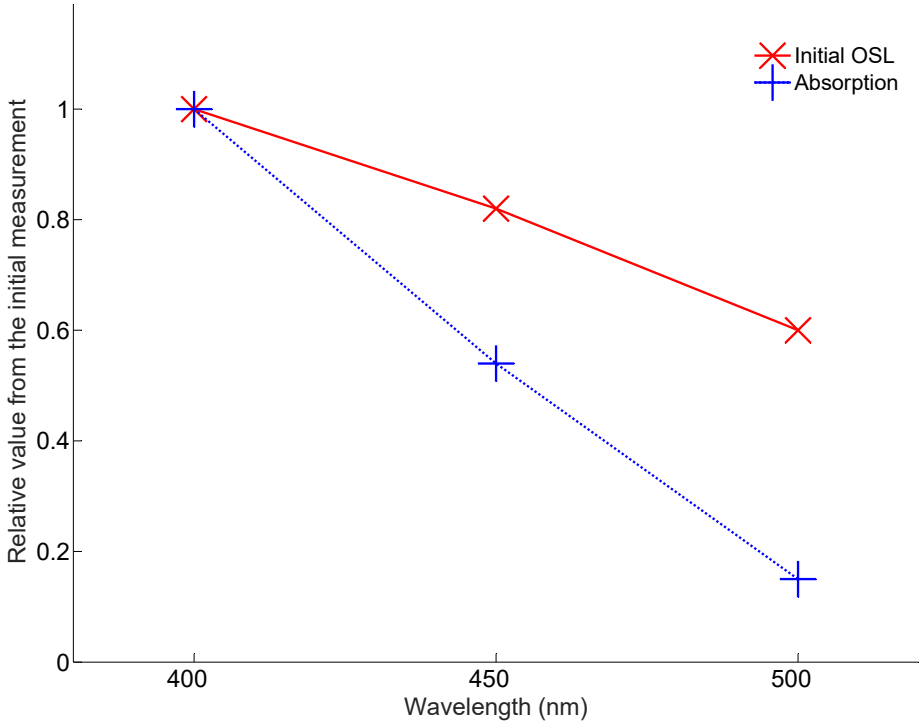

Figure 4.9. This figure shows the comparison between OSL and absorption spectrum of the irradiated LTB:Ag. The absorption plotted here are the relative differences between the absorption coefficient at each of the stimulation wavelengths and the trough at 564 nm (2.2 eV in Figure 4.2).

because the mechanisms between OSL and absorption processes are different from each other. Also, the lamp output for the Cary spectrophotometer and the Fluorolog spectrofluorometer are not the same; therefore, the Fluorolog spectrofluorometer, with the stronger light between the two, would cause more light to be emitted. Another possible explanation for the higher OSL values is because there are other underlying absorption bands on the shorter wavelength side of the 370 nm as mentioned in the last section, that may cause more luminescence.

4.3.2 Spectral Dependence of OSL Emission

To determine the emission wavelength of the OSL with 400 nm stimulation, a series of PL scans were conducted while the excitation lamp was kept on. The Fluorolog was set to monitor 235 to 315 nm in second order (470 to 630 nm) with the excitation

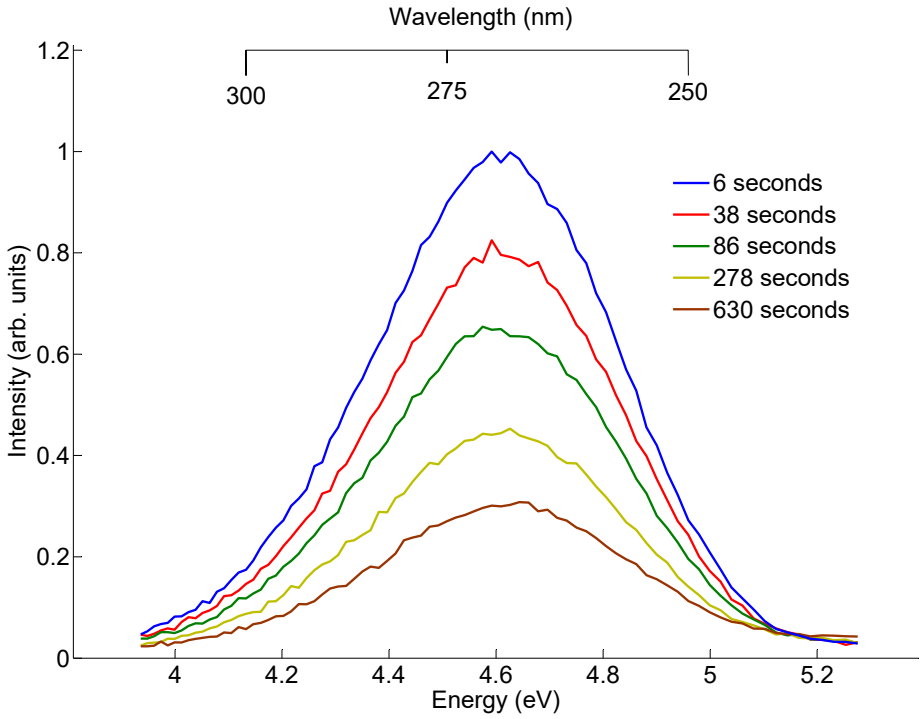

Figure 4.10. Spectral dependence of OSL emission. The order of the curves from top to bottom correspond to the increase in the excitation time. The times indicated are the estimated time at the peak of each curve.

and emission slits at 10 and 5 nm, integration time of 0.1 s, and increment of 2 nm. Each scan took 12 s and the reset time between scans was about 4 s. Figure 4.10 shows five of the forty scans taken. The figure shows an emission of approximately 270 nm throughout the OSL. The emission is the same as the PL in Figure 4.1. The FWHM of the first and last curves are 0.58 eV, which are comparable to that of the PL band with 0.54 eV. The emission of 270 nm is a characteristic of excited Ag^{+} ions, seen in Section 4.1, de-exciting to the ground state. This means that 400 nm absorption, previously attributed to the Ag_i^0, moved trapped electrons to the conduction band, and those electrons then recombined with Ag_{Li}^{2+} centers, creating excited states of $Ag_{Li}^{+}(4d^9 5s)$. The main process of OSL can be simply illustrated like a one trap one recombination center model drawn in Figure 4.11, where Ag_i^0 is the electron trap and the Ag_{Li}^{2+} is the recombination center. The following summarizes the OSL with 400 nm stimulation:

Irradiation

1. $e^- + Ag_i^+ \rightarrow Ag_i^0$ (trapped electron)
2. $h^- + Ag_{Li}^+ \rightarrow Ag_{Li}^{2+}$ (trapped hole)

Stimulation $Ag_i^0 + h\nu$ (400 nm photon) $\rightarrow Ag_i^+ +$ released e^-

Emission $e^- + Ag_{Li}^{2+} \rightarrow (Ag_{Li}^+)^* \rightarrow Ag_{Li}^+ + h\nu$ (270 nm photon).

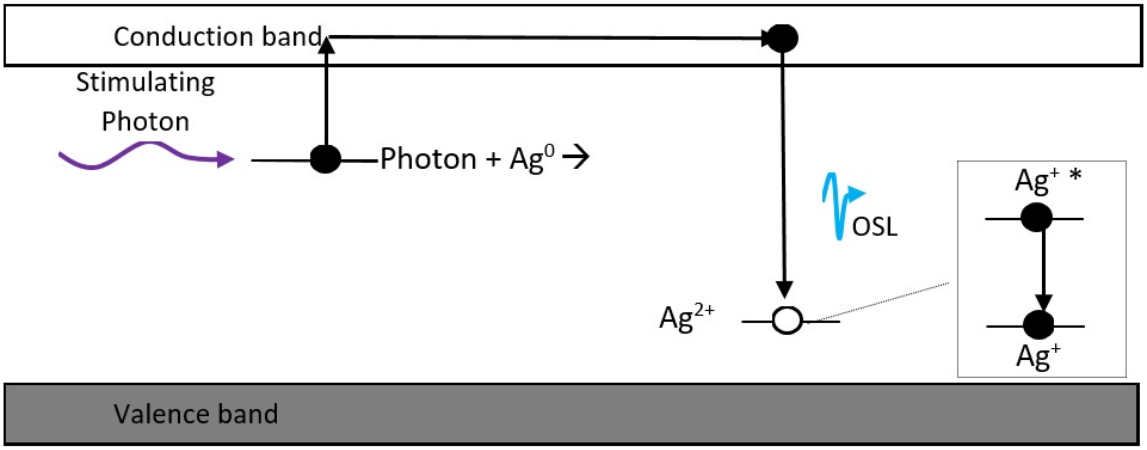

Figure 4.11. OSL OTOR model for the 400 nm excitation

4.3.3 Effects of Excitation Photon Flux on OSL

The photon intensity f $[cm^2]$, discussed in Section 2.2, of the stimulating light is greater with the diode laser than with the xenon lamp. Recall that f is proportional to the photon flux ϕ. With the procedures from Section 3.3.5, two piecewise OSL spectra were collected with the Fluorolog spectrofluorometer using kinetics mode. The excitation and emission slits were set at 10 and 5 nm, respectively. The integration time was 0.5 s. The emission was monitored at the second order of 270 nm (540 nm). One OSL was with 405 nm laser stimulation, and the other was with 400 nm stimulation from the xenon lamp. The initial OSL intensity from the laser was 12 times greater than the xenon lamp (see Appendix B). The results were normalized to the initial OSL intensity (0 s) of each and shown in Figure 4.12. The background[2] from the scattered light was also removed from the intensity. Oxygen vacancies are involved in creating the discontinuities between segments of the OSL with the laser stimulation. According to Swinney *et al.* paramagnetic oxygen vacancies have a characteristic 4-line EPR spectrum due to a hyperfine interaction with one ^{11}B

[2]Background was determined from running kinetics experiment without the sample for each of the stimulation sources.

neighbor [16]. B. E Kananen saw the same 4-line EPR spectrum that was convoluted in the Ag_i^0 EPR lines when he shined the 405 nm diode laser in the EPR cavity with the x-ray irradiated LTB:Ag. The effect of doing this decreased the Ag_i^0 lines but increased the 4-line oxygen vacancy signals. The signals from the oxygen vacancies slowly decayed at room temperature as the electrons were released thermally, when the laser was shut off. The time determined for these traps to decay was about 5 to 10 minutes, and hence, 6 minutes was chosen as the time for rest between the OSL steps. Some of the electrons from oxygen were re-trapped to make more Ag_i^0 centers which were evident in the EPR signals as the lines increased in magnitude. Some recombined at the hole centers emitting small amounts of light (see Appendix C).

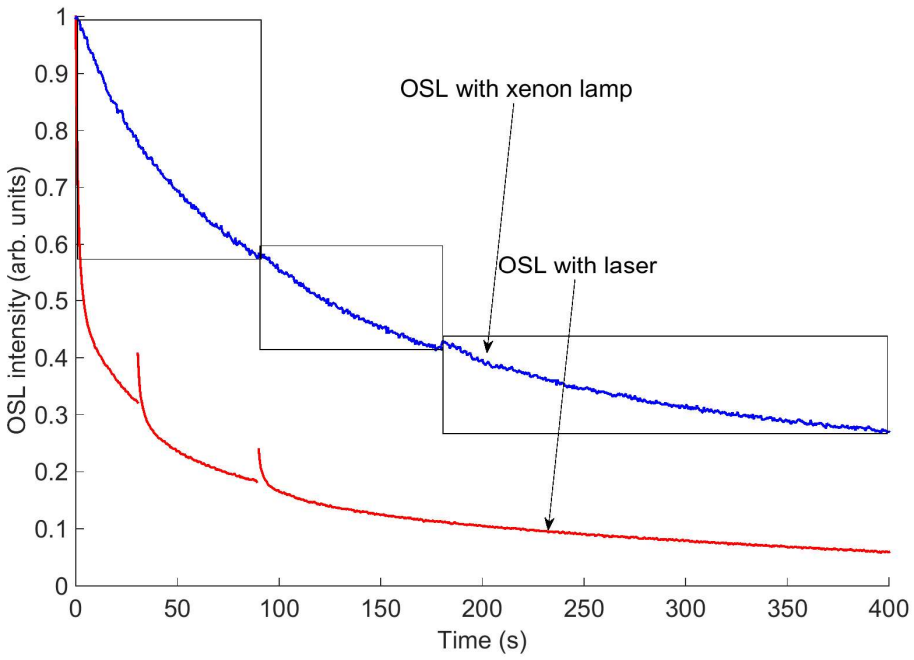

Figure 4.12. OSL with 405 nm diode laser and xenon lamp at 400 nm. The boxes are drawn on the traces of OSL with xenon lamp, to show the 90 s, 90 s, and up to 600 s segments between which were latency periods of 6 minutes without stimulation. For the laser OSL, the discontinuities are obvious between segments of 30 s, 60 s, and up to 600 s total stimulation. The actual initial intensity of the laser OSL was 12 times higher than the initial of the xenon lamp OSL (see Appendix C, Figure C.3). Both OSL curves were normalized here to emphasize the different decay rates.

With oxygen vacancies, more terms need to be included in the system of rate equations, making it different from the OSL OTOR model. I propose the following rate equations for the stimulation stage:

$$
\begin{aligned}
-\frac{dm}{dt} &= A_m m n_c = I_{OSL}, && (34)\\
\frac{dv}{dt} &= A_v(V-v)n_c - s\cdot v\cdot exp(-\frac{E}{kT}), && (35)\\
\frac{dn}{dt} &= -fn + A_n(N-n)n_c, && (36)\\
\frac{dn_c}{dt} &= \frac{dm}{dt} - \frac{dn}{dt} - \frac{dv}{dt}. && (37)
\end{aligned}
$$

In (35), V and v are the capacity of oxygen vacancies and its occupancy in time, and A_v is its probability of trapping electrons. This equation also assumes that trapped electrons at oxygen vacancies are only thermally released, so it has no f term. Trapped electrons in the oxygen vacancies are thermally release at a rate equal to $s \cdot v \cdot exp(-E/kT)$, where E and s are the activation energy and frequency factor associated with oxygen vacancies. Recall that (5) and (6) are the same as (34) and (36). Equation (37) is only different from (7) by $-\frac{dv}{dt}$. Basically, the system is made of OSL and TL models combined.

The large photon intensity, f, from the laser was crucial in revealing the effects of oxygen vacancies. Not only does large f mean that more electrons are being released and recombining, but also, more of them are being trapped at the oxygen vacancies at some probability that is smaller than the probability of recombining to produce OSL (i.e., $A_v < A_m$). When the light is off, the electrons at oxygen vacancies are released at room temperature, and are either trapped at Ag_i^{+} or recombined with Ag_{Li}^{2+} ions. When the stimulation is turned on again, the intensity of OSL is increased because the electron traps were "recharged". With the xenon lamp, the slow decay means slower recombination rate, and also, fewer electrons being trapped at oxygen vacancies. The

few electrons that get trapped are immediately released during the OSL readout, so when the light is off, there are far fewer electrons in the oxygen vacancies to recharge Ag_i^+ traps. That is why there are hardly any discontinuities between segments of OSL with xenon.

4.3.4 OSL with 325 nm Stimulation

In seeking the underlying band on the shorter side of the 370 nm peak, an excitation near 325 nm was serendipitously observed to emit high OSL intensity. This discovery was made by taking a PLE scan of the irradiated crystal while monitoring emission at 270 nm. Using the same parameters as in the previous OSL runs, the result of the 325 nm stimulation gave intensities higher than the OSL with 400 nm stimulation by a factor of 2.7 (see Appendix B). Brant *et al.* reported that 297 and 325 nm excitation on irradiated LTB:Ag crystals each give PL of 510 nm and 725 nm, respectively. He proposed that these originate from the charge transfer of an electron from nearby oxygen ions to hole centers of Ag_{Li}^{2+} [35]. The 325 nm stimulation was specifically associated with the perturbed hole centers. Perhaps, the 325 nm could cause an electron to mobilize from Ag_i^0 to an unperturbed Ag_{Li}^{2+}(as with the 400 nm stimulation), as well as, mobilize a hole in the valence band that starts from an oxygen transferring its electron to the perturbed Ag_{Li}^{2+}. With both perturbed and unperturbed hole centers participating, higher OSL intensity could result. This subject is worth examining in another set of EPR and optical experiments to determine the exact cause. The high intensity from 325 nm stimulation is promising to the dosimetry industry.

V. Conclusion

5.1 Discussion and Way Ahead

It has been shown that OSL is present in x-ray irradiated lithium tetraborate crystals doped only with silver. There was sufficient OSL when 400 nm light freed electrons from Ag_i^0 atoms that recombined with Ag_{Li}^{2+} ions. There is the question of being able to replicate this OSL with other samples of LTB with different silver concentrations. Obtaining pure LTB and diffusing it with silver in a furnace could be the next step forward to understanding the OSL further. Also, studies of absolute concentrations of traps, along with OSL readouts, may help in determining the coefficients of the system of rate equations. Simulation of OSL may be done in a computer program by solving the equations numerically.

The presence of more than one trap complicates the application of LTB:Ag as a dosimeter. The presence of oxygen vacancies competing with the recombination centers diminishes the OSL intensity and could lead to false measurement of radiation dosage absorbed by the crystal. For example, if LTB:Ag is to be used in POSL with a powerful 400 nm stimulation light for a fraction of a second, it must be noted that oxygen vacancies could lower the intensity of the luminescence. If used in DOSL, the delay in reading the intensity must also account for the thermal release rate of the electrons from oxygen vacancies.

The absorption bands of LTB:Ag are not fully understood. There are the peaks near 650, 300, and 250 nm that cannot be assigned to defects. The additional CW-OSL experiment at 325 nm showed higher OSL intensity, but the 325 nm excitation was not seen in the optical absorption spectra as a significant peak. In order to understand the other absorption bands and determine their locations exactly, the crystal must be examined at liquid nitrogen temperatures (77 K) to get better resolution for

the absorption. For the 325 nm OSL stimulation, a correlation experiment between bleaching, with a laser near 325 nm, and the change in the EPR lines of the hole traps under cold temperature may give better insight on the mechanism of the OSL at this stimulation wavelength.

5.2 Summary

The experiments in this thesis showed the presence of Ag^+ ions in the one crystal examined. The PL near 270 nm and PLE near 205 nm proves their existence, in accordance with previous research in literature. Both the absorption spectra of the pre-irradiated and x-ray irradiated crystal show the absorption of the Ag^+ ions at 205 nm as well.

The x-ray irradiated absorption spectrum showed multiple peaks aside from the Ag^+ ions near 250, 300, 370, and 650 nm. The most broad beak near 370 nm was shown to decay with bleaching light at 400 nm. The other absorption bands at 650 nm, 300 nm, 250 nm were not examined closely, and therefore, these were not assigned to specific defects. Emphasis of this thesis was on the 370 nm absorption, and EPR studies showed that the decrease in the magnitude of the signals from Ag_i^0 (trapped-electron center) correlated with the decrease in the 370 nm absorption band, with 400 nm bleaching light. Additionally, the EPR signal of unperturbed hole traps of Ag_{Li}^{2+} also decreased. This led to the conclusion that 400 nm light stimulates the Ag_i^0 centers, to release electrons into the conduction band. Then the electrons mostly recombine with Ag_{Li}^{2+}, and a few get trapped at oxygen vacancies.

The OSL from 400 nm stimulation is explained by electrons recombining with Ag_{Li}^{2+}, to form Ag_{Li}^{+} ions. The electrons have a tendency to recombine at unperturbed Ag_{Li}^{2+} hole sites. The spectral dependence of OSL emission shows a steady emission at 270 nm through time, similar to the PL of Ag^+. This indicates that Ag_{Li}^{+}

excites and de-excites, as in the PL of the pre-irradiated crystal, after recombination.

The effects of oxygen vacancies were more apparent with the use of 405 nm diode laser. When piecewise OSL readings were taken with 6 minutes of rest in between readouts with no laser light, discontinuities in the OSL traces were seen. The discontinuities were due to oxygen vacancies trapping free electrons, and subsequently, releasing some of them back to the Ag_i^+ (electron traps) to produce more trapped states, Ag_i^0. As a result, when stimulating light is on again, the intensity of the OSL is increased from when the stimulation was last shut off.

Stimulation with 400 nm is not the only source of OSL. Later in the research period, a more intense OSL with 325 nm stimulation was discovered. This involves the perturbed hole centers and may be different from the OSL process with 400 nm light. This is worth looking into in the future.

Appendix A. Spectrofluorometer Spectral Response Corrections

The system response (or spectral response) of a monochromator causes an apparent shift of emission peaks from actual wavelengths. This is due to the fact that when the monitored light goes through a series of mirrors and diffraction gratings to the photomultiplier tube (PMT), there will be discrepancies between the intensities read and the actual intensities. In other words, the instrument will respond differently at different wavelengths. This can be seen in Figure A.1, for the PMT. The decline in the radiant sensitivity from 300 to 200 nm of the R928 PMT, makes it inadequate in monitoring wavelengths in this range.

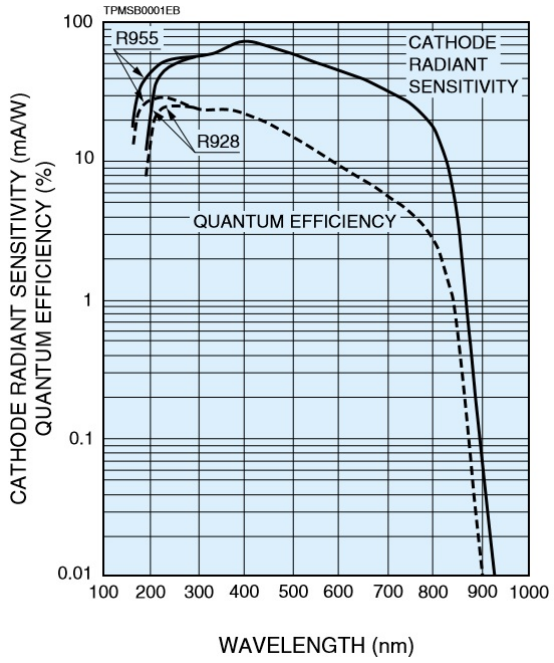

Figure A.1. Photomultiplier tube (PMT) spectral response. There is a significant drop-off of the solid curve for R928 from 300 nm to 200 nm in radiant sensitivity. The figure is taken with permission from Hamamatsu [48].

As outlined by Lakowicz, spectral response can be obtained by a detector that measures the output of a source lamp at different wavelengths, $L(\lambda)$. The PMT would measure the intensity, $I(\lambda)$, of the same light. This intensity is related to the system

response, $S_{response}(\lambda)$, by [39:53],

$$I(\lambda) = L(\lambda)S_{response}(\lambda). \tag{38}$$

In literature, a sintered polytetrafluoroethylene (PTFE) diffused reflector was used as the calibrating sample [38], but in our experiment, we used the LTB:Ag annealed and pre-irradiated, under the assumption that the same wavelengths as the excitation beam would be scattered off the crystal for the emission spectrometer. A

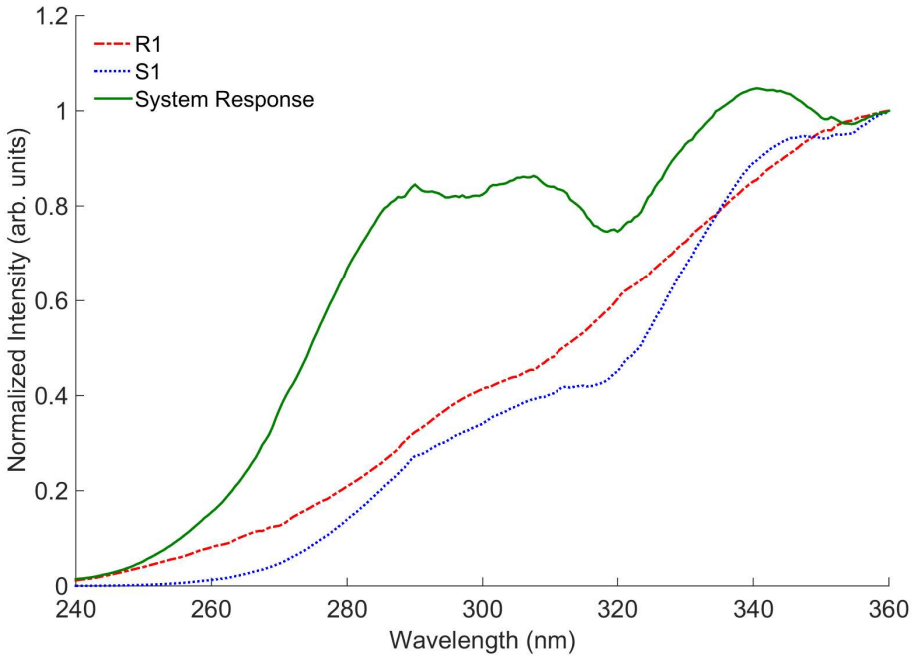

Figure A.2. Synchronous scan of S1 and R1 detectors. Each of the spectra is normalized, then the ratios of the two S1/R1 was taken to be the system response, $S_{response}(\lambda)$.

synchronous scan was conducted with the R1 (photodiode) and S1 (photomultiplier tube) detectors activated. The idea is that R1 would represent the $L(\lambda)$, and the S1 the $I(\lambda)$. Recall, R1 and S1 detectors have different units. To overcome this difference, the values were normalized to the highest values in each of the curves. These ratios of the normalized data, $I(\lambda)/L(\lambda)$ or S1/R1 were then taken to be the

system response correction values, $S_{response}(\lambda)$. The result of the synchronous scan is shown in Figure A.2.

The system response values were then taken to correct the photoluminescence of the pre-irradiated LTB:Ag crystal excited at 205 nm, shown in Figure A.3. Each

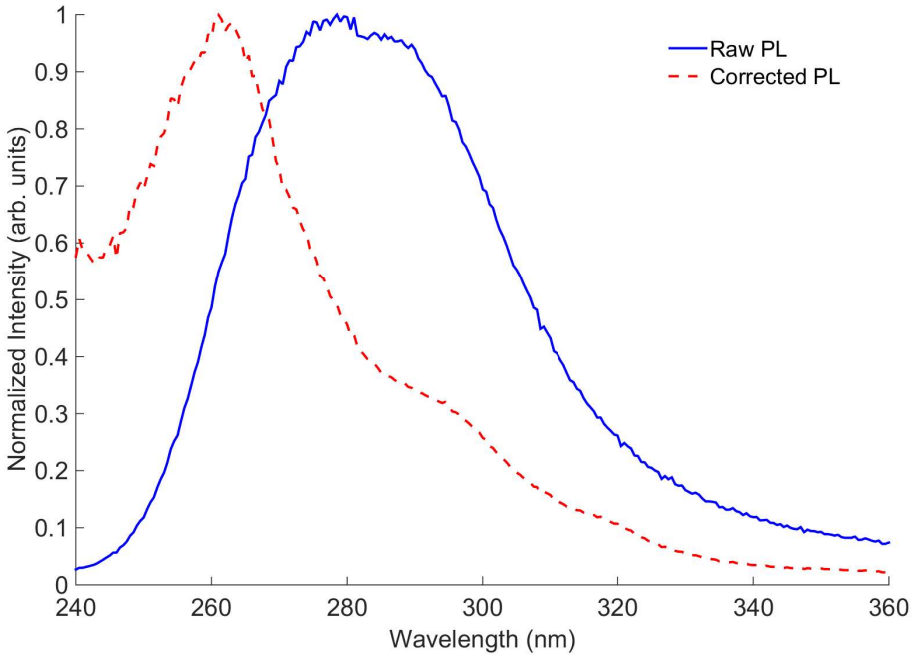

Figure A.3. Inadequate system response correction of a PL spectrum. This is from a pre-irradiated LTB:Ag. The raw PL spectrum shows a peak near 280 nm. The corrected PL shows the shift of the peak to around 260 nm, after applying the system response correction.

element obtained from the S1 detector, $I(\lambda)$, and $S_{response}(\lambda)$ were divided at each wavelength increment,

$$I_{corrected}(\lambda) = I(\lambda)/S_{response}(\lambda)$$

to get the corrected values. When plotted, the corrected curve was supposed to be closer to the actual. The emission peak was close to 267 nm as reported in literature [10, 41, 42]; however, the corrected emission was deformed. It required

complex mathematical manipulation that could distort the results even further. It was determined that this method was not the best for spectral response correction because the emission spectrometer was inefficient below 300 nm. This procedure may be useful for monitoring wavelengths above 300 nm, but in this thesis, it was not used. Instead, emission at the wavelengths of interest were monitored at second-order diffraction, which gave data with high signal-to-noise ratios.

Appendix B. Raw Data from OSL Stimulating at 325, 400, 450, 500, and 650 nm

The figure below shows the raw OSL data as read by the Fluorolog spectrofluorometer. The thesis only focused on the 400-500 nm stimulation traces, which are discussed in Section 4.3.1.

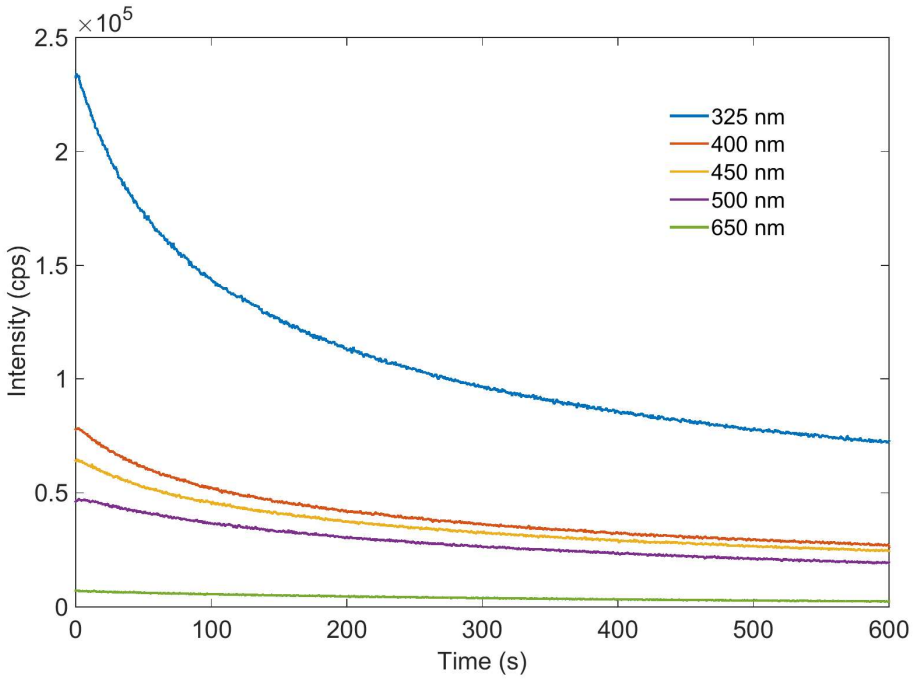

Figure B.1. Raw data from OSL at 325, 400, 450, 500, 650 nm of stimulation.

Appendix C. Raw Data From OSL With Laser and Xenon Lamp

The figures below show the raw data from the piecewise OSL runs with the laser and xenon lamp stimulation. Figure C.1 is the only one of its kind showing the small amounts of luminescence when the stimulating light was blocked for 6 minutes. These luminescence curves are enlarged in Figure C.2 and are caused by electrons releasing from oxygen vacancies and recombining at the hole centers.

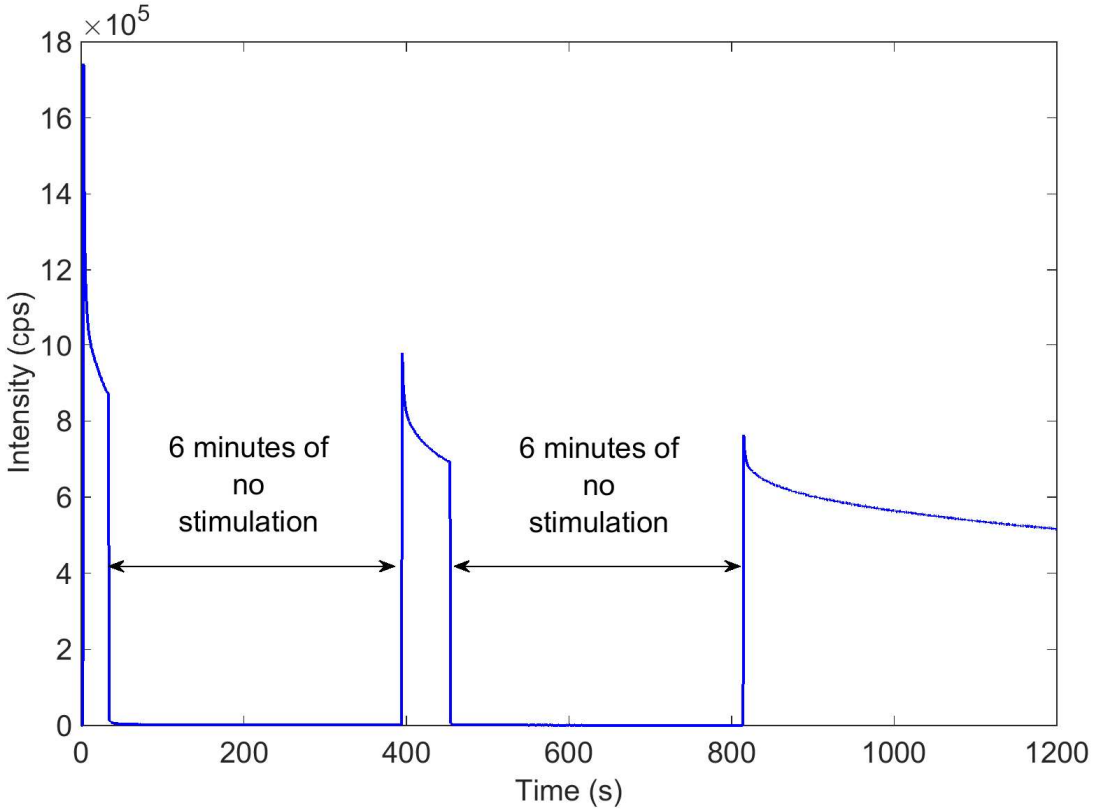

Figure C.1. Raw data of OSL with 405 nm laser including the segments of 6 minutes of no stimulation. The background from scattered light was not removed, making OSL traces appear higher. The background was determined to be approximately 4.5×10^5 cps.

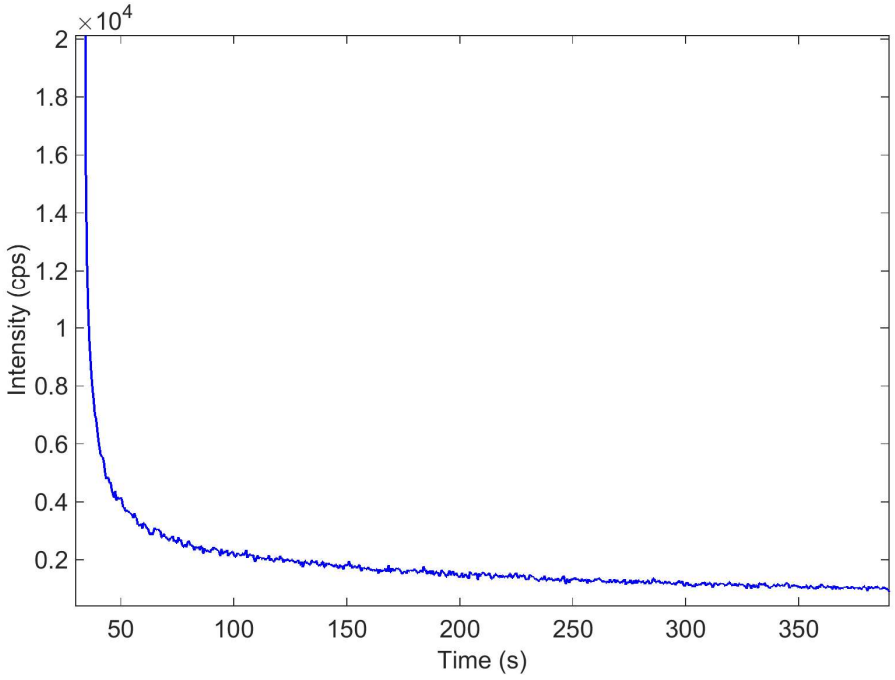

(a)

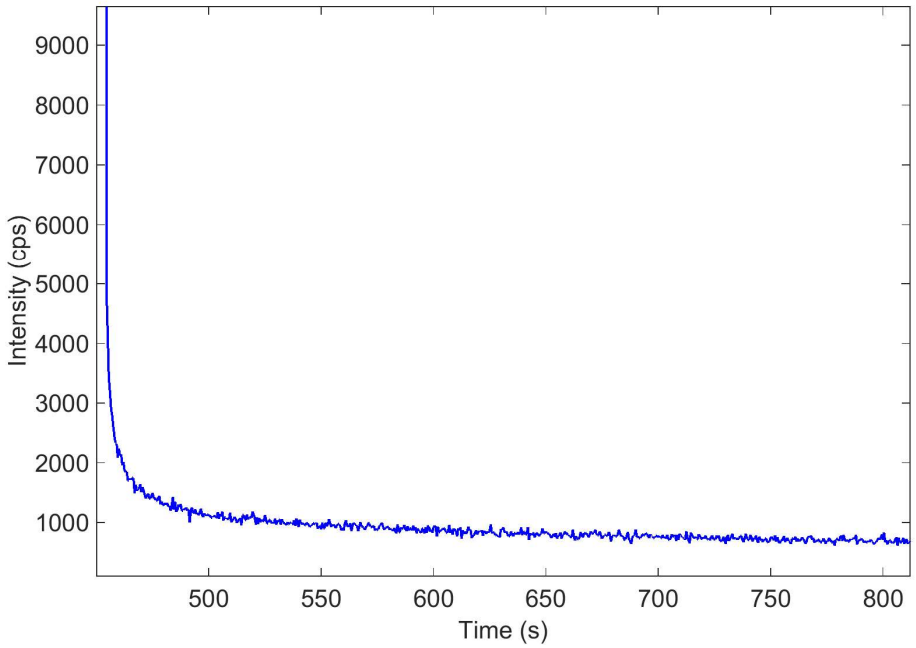

(b)

Figure C.2. Very small luminescence from the oxygen vacancies at room temperature in the (a) first, and (b) second segments of six minutes of no stimulation, enlarged from Figure C.1.

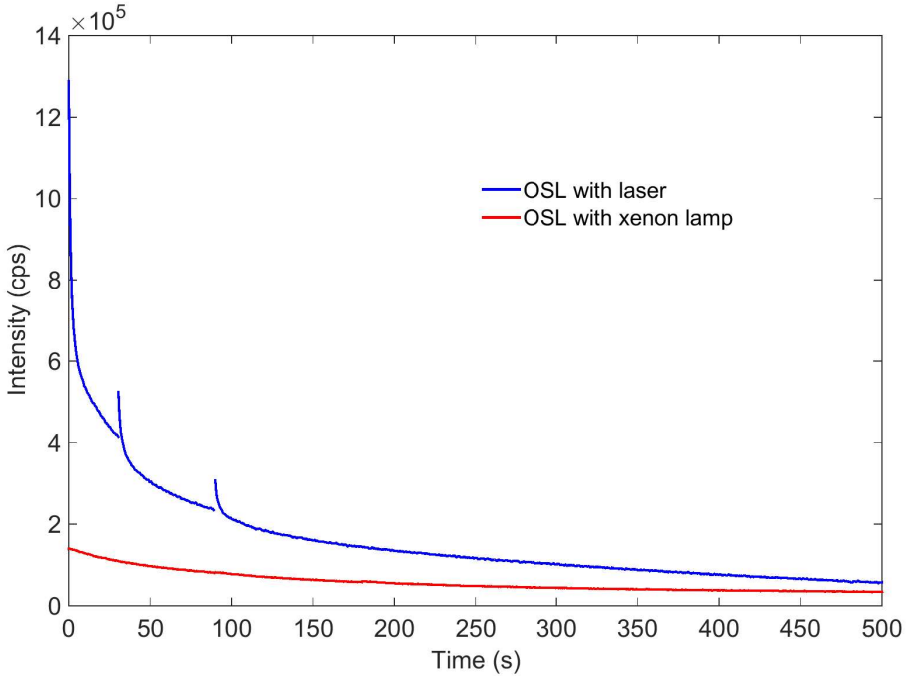

Figure C.3. Raw data of OSL traces with the laser and xenon lamp, with the background scattering and the segments of no stimulation removed. Normalized plots of these can be seen in Figure 4.12.

Bibliography

1. B. S. R. Sastry and F. A. Hummel, "Studies in Lithium Oxide Systems: I, Li_2O B_2O_3-B_2O_3," *Journal of the American Ceramic Society*, vol. 41, no. 1, pp. 7–17, 1958.

2. J. Krogh-Moe, "The crystal structure of lithium diborate, $Li_2O{\cdot}_2B_2O_3$," *Acta Crystallographica*, vol. 15, no. 3, pp. 190–193, 1962.

3. J. Krogh-Moe, "Refinement of the crystal structure of lithium diborate $Li_2O{\cdot}_2B_2O_3$," *Acta Crystallographica Section B: Structural Crystallography and Crystal Chemistry*, vol. 24, no. 2, pp. 179–181, 1968.

4. A. Bhalla, L. Cross, and R. Whatmore, "Pyroelectric and piezoelectric properties of lithium tetraborate single crystal," *Japanese Journal of Applied Physics*, vol. 24, no. S2, p. 727, 1985.

5. R. Komatsu, T. Sugawara, K. Sassa, N. Sarukura, Z. Liu, S. Izumida, Y. Segawa, S. Uda, T. Fukuda, and K. Yamanouchi, "Growth and ultraviolet application of $Li_2B_4O_7$ crystals: Generation of the fourth and fifth harmonics of Nd:$Y_3Al_5O_{12}$ lasers," *Applied Physics Letters*, vol. 70, no. 26, pp. 3492–3494, 1997.

6. T. Sugawara, R. Komatsu, and S. Uda, "Linear and nonlinear optical properties of lithium tetraborate," *Solid State Communications*, vol. 107, no. 5, pp. 233–237, 1998.

7. Y. Ebata and M. Koshino, "SAW Resonator and Resonator Filter on $Li_2B_4O_7$ Substrate," *Japanese Journal of Applied Physics*, vol. 26, no. S1, p. 123, 1987.

8. B. E. Kananen, "Neutron Induced Defects in Isotopically Enriched Lithium Tetraborate," Master's thesis, Air Force Institute of Technology, March 2011.

9. C. Furetta, M. Prokic, R. Salamon, V. Prokic, and G. Kitis, "Dosimetric characteristics of tissue equivalent thermoluminescent solid TL detectors based on lithium borate," *Nuclear Instruments and Methods in Physics Research, Section A: Accelerators, Spectrometers, Detectors and Associated Equipment*, vol. 456, no. 3, pp. 411–417, 2001.

10. N. Rawat, M. Kulkarni, M. Tyagi, P. Ratna, D. Mishra, S. Singh, B. Tiwari, A. Soni, S. Gadkari, and S. Gupta, "TL and OSL studies on lithium borate single crystals doped with Cu and Ag," *Journal of Luminescence*, vol. 132, no. 8, pp. 1969–1975, 2012.

11. B. Tiwari, N. Rawat, D. Desai, S. Singh, M. Tyagi, P. Ratna, S. Gadkari, and M. Kulkarni, "Thermoluminescence studies on Cu-doped $Li_2B_4O_7$ single crystals," *Journal of Luminescence*, vol. 130, no. 11, pp. 2076–2083, 2010.

12. M. Takenaga, O. Yamamoto, and T. Yamashita, "Preparation and characteristics of $Li_2B_4O_7$: Cu phosphor," *Nuclear Instruments and Methods*, vol. 175, no. 1, pp. 77–78, 1980.

13. M. Danilkin, I. Jaek, M. Kerikmäe, A. Lust, H. Mändar, L. Pung, A. Ratas, V. Seeman, S. Klimonsky, and V. Kuznetsov, "Storage mechanism and OSL-readout possibility of $Li_2B_4O_7$: Mn (TLD-800)," *Radiation Measurements*, vol. 45, no. 3-6, pp. 562–565, 2010.

14. S. McKeever and M. Moscovitch, "Topics under Debate-On the advantages and disadvantages of optically stimulated luminescence dosimetry and thermoluminescence dosimetry," *Radiation protection dosimetry*, vol. 104, no. 3, pp. 263–270, 2003.

15. N. Sennova, R. Bubnova, G. Cordier, B. Albert, S. Filatov, and L. Isaenko, "Temperature-dependent Changes of the Crystal Structure of $Li_2B_4O_7$," *Zeitschrift für anorganische und allgemeine Chemie*, vol. 634, no. 14, pp. 2601–2607, 2008.

16. M. W. Swinney, J. W. McClory, J. C. Petrosky, S. Yang, A. T. Brant, V. T. Adamiv, Y. V. Burak, P. A. Dowben, and L. E. Halliburton, "Identification of electron and hole traps in lithium tetraborate (Li2B4O7) crystals: Oxygen vacancies and lithium vacancies," *Journal of Applied Physics*, vol. 107, no. 11, p. 113715, 2010.

17. V. Adamiv, Y. Burak, and I. Teslyuk, "The crystal structure of $Li_2B_4O_7$ compound in the temperature range 10-290K," *Journal of Alloys and Compounds*, vol. 475, no. 1-2, pp. 869–873, 2009.

18. "Diamond® 3.0 software. Crystal Impact."

19. A. Ratas, M. Danilkin, M. Kerikmäe, A. Lust, H. Mändar, V. Seeman, and G. Slavin, "$Li_2B_4O_7$:Mn for dosimetry applications: traps and mechanisms," *Proceedings of the Estonian Academy of Sciences*, vol. 61, no. 4, pp. 279–295, 2012.

20. F. Agullo-Lopez, *Point Defects in Materials*. San Diego, CA: Academic Press Limited, 1988.

21. E. G. Yukihara and S. W. S. McKeever, *Optically Stimulated Luminescence, Fundamentals and Applications*. West Sussex, UK: John Wiley & Sons Ltd, 2011.

22. R. Chen and P. Leung, "Dose dependence and dose-rate dependence of the optically stimulated luminescence signal," *Journal of Applied Physics*, vol. 89, no. 1, pp. 259–263, 2001.

23. H. Grimmeiss and L. Ledebo, "Photo-ionization of deep impurity levels in semiconductors with non-parabolic bands," *Journal of Physics C: Solid State Physics*, vol. 8, no. 16, pp. 2615–2626, 1975.

24. D. J. Huntley, D. I. Godfrey-Smith, and M. L. Thewalt, "Optical dating of sediments," *Nature*, vol. 313, no. 5998, pp. 105–107, jan 1985.

25. M. S. Akselrod and S. W. S. Mckeever, "A Radiation Dosimetry Method Using Pulsed Optically Stimulated Luminescence," vol. 81, no. 3, pp. 167–176, 1999.

26. R. Yoder and M. Salasky, "A dosimetry system based on delayed optically stimulated luminescence," *The Health Phys Society*, vol. 72, pp. S18–S19, 1997.

27. E. Bulur, "An alternative technique for optically stimulated luminescence (OSL) experiment," *Radiation Measurements*, vol. 26, no. 5, pp. 701–709, 1996.

28. R. Chen and V. Pagonis, *Thermally and Optically Stimulated Luminescence: A Simulation Approach*. West Sussex, UK: John Wiley & Sons Ltd, 2011.

29. M. Fox, *Optical Properties of Solids*, 2nd ed. Oxford, UK: Oxford University Press, 2010.

30. P. F. Bernath, *Spectra of Atoms and Molecules*, 2nd ed. Oxford: Oxford University Press, 2005.

31. B. Henderson and G. Imbusch, *Optical Spectroscopy of Inorganic Solids*, 2nd ed. Oxford, UK: Oxford Science Publications, 1989.

32. M. de Jong, L. Seijo, A. Meijerink, and F. T. Rabouw, "Resolving the ambiguity in the relation between Stokes shift and Huang–Rhys parameter," *Physical Chemistry Chemical Physics*, vol. 17, no. 26, pp. 16 959–16 969, 2015.

33. J. A. Weil and J. R. Bolton, *Electron Paramagnetic Resonance: Elementary Theory and Practical Applications*, 2nd ed. Hoboken, NJ: John Wiley & Sons Ltd, 2007.

34. A. T. Brant, B. E. Kananan, M. K. Murari, J. W. McClory, J. C. Petrosky, V. T. Adamiv, Y. V. Burak, P. A. Dowben, and L. E. Halliburton, "Electron and hole traps in Ag-doped lithium tetraborate ($Li_2B_4O_7$) crystals," *Journal of Applied Physics*, vol. 110, 2011.

35. A. T. Brant, D. A. Buchanan, J. W. McClory, V. T. Adamiv, Y. V. Burak, L. E. Halliburton, and N. C. Giles, "Photoluminescence from Ag^{2+} ions in lithium tetraborate ($Li_2B_4O_7$) crystals," *Journal of Luminescence*, vol. 153, pp. 79–84, 2014.

36. *Fluorolog®-3 How to Build a Spectrofluorometer*, 2013.

37. *Fluorolog®-3 Operation Manual*, 2002.

38. P. C. DeRose, E. A. Early, and G. W. Kramer, "Qualification of a fluorescence spectrometer for measuring true fluorescence spectra," *Review of Scientific Instruments*, vol. 78, no. 3, p. 033107, 2007.

39. J. R. Lakowicz, *Principles of Fluorescence Spectroscopy*, 2nd ed. Baltimore, MD: Springer, 2006.

40. A. Kelemen, M. Ignatovych, V. Holovey, T. Vidoczy, and P. Baranyai, "Effect of irradiation on photoluminescence and optical absorption spectra of $Li_2B_4O_7$: Mn and $Li_2B_4O_7$: Ag single crystals," *Radiation Physics and Chemistry*, vol. 76, no. 8, pp. 1531–1534, 2007.

41. G. D. Patra, M. Tyagi, D. G. Desai, B. Tiwari, S. Sen, and S. C. Gadkari, "Photo-luminescence properties of Cu and Ag doped $Li_2B_4O_7$ single crystals at low temperatures," *Journal of Luminescence*, vol. 132, no. 5, pp. 1101–1105, 2012.

42. G. D. Patra, S. G. Singh, B. Tiwari, S. Sen, D. G. Desai, and S. C. Gadkari, "Thermally stimulated luminescence process in copper and silver co-doped lithium tetraborate single crystals and its implication to dosimetry," *Journal of Luminescence*, vol. 137, pp. 28–31, 2013.

43. M. Dergachev, V. Moiseenko, and Y. V. Burak, "Raman scattering in $Li_2B_4O_7$ crystals with impurities," *Optics and Spectroscopy*, vol. 90, no. 4, pp. 534–537, 2001.

44. J. Pickering and V. Zilio, "New accurate data for the spectrum of neutral silver," *The European Physical Journal D-Atomic, Molecular, Optical and Plasma Physics*, vol. 13, no. 2, pp. 181–185, 2001.

45. C. Sousa, C. de Graaf, F. Illas, M. T. Barriuso, J. A. Aramburu, and M. Moreno, "Neutral atoms in ionic lattices: Excited states of $KCl : Ag^0$," *Physical Review B*, vol. 62, pp. 13 366–13 375, Nov 2000.

46. D. A. Buchanan, M. S. Holston, A. T. Brant, J. W. McClory, V. T. Adamiv, Y. V. Burak, and L. E. Halliburton, "Electron paramagnetic resonance and thermoluminescence study of Ag^{2+} ions in $Li_2B_4O_7$ crystals," *Journal of Physics and Chemistry of Solids*, vol. 75, no. 12, pp. 1347–1353, 2014.

47. A. T. Brant, D. A. Buchanan, J. W. McClory, P. A. Dowben, V. T. Adamiv, Y. V. Burak, and L. E. Halliburton, "EPR identification of defects responsible for thermoluminescence in Cu-doped lithium tetraborate ($Li_2B_4O_7$) crystals," *Journal of Luminescence*, vol. 139:, pp. 125–131, 2013.

48. *Photomultiplier Tube R928, R955*. [Online]. Available: http://www.hamamatsu.com/us/en/R928.html

REPORT DOCUMENTATION PAGE

Form Approved
OMB No. 0704–0188

1. REPORT DATE (DD–MM–YYYY)	**2. REPORT TYPE**	**3. DATES COVERED** (*From — To*)
24-03-2016	Master's Thesis	October 2014 – March 2016

4. TITLE AND SUBTITLE

Optically Stimulated Luminescence from Ag-doped Lithium Tetraborate ($Li_2B_4O_7$)

5a. CONTRACT NUMBER

5b. GRANT NUMBER

5c. PROGRAM ELEMENT NUMBER

6. AUTHOR(S)

Maniego, Ember S., MAJ, USA

5d. PROJECT NUMBER

5e. TASK NUMBER

5f. WORK UNIT NUMBER

7. PERFORMING ORGANIZATION NAME(S) AND ADDRESS(ES)
Air Force Institute of Technology
Graduate School of Engineering and Management (AFIT/EN)
2950 Hobson Way
WPAFB OH 45433-7765

8. PERFORMING ORGANIZATION REPORT NUMBER

AFIT-ENP-MS-16-M-075

9. SPONSORING / MONITORING AGENCY NAME(S) AND ADDRESS(ES)

POC: MAJ Andrew Decker (andrew.w.decker.mil@mail.mil)
Defense Threat Reduction Agency
8725 John. J. Kingman Rd
Ft. Belvoir, VA 22060

10. SPONSOR/MONITOR'S ACRONYM(S)

DTRA

11. SPONSOR/MONITOR'S REPORT NUMBER(S)

12. DISTRIBUTION / AVAILABILITY STATEMENT

DISTRIBUTION STATEMENT A:
APPROVED FOR PUBLIC RELEASE; DISTRIBUTION UNLIMITED.

13. SUPPLEMENTARY NOTES

14. ABSTRACT

Silver-doped lithium tetraborate ($Li_2B_4O_7$) crystals emit optically stimulated luminescence (OSL) in response to stimulating light around 400 nm. Photoluminescence, optical absorption, and electron paramagnetic resonance (EPR) were used to identify the defects in the crystal that cause this OSL. Lithium tetraborate crystals have Ag^+ ions at Li^+ sites and at interstitial sites. Upon ionization at room temperature via x rays, electron-hole pairs are generated. The electrons are trapped at Ag^+ occupying interstitial sites, while the holes are trapped at Ag^+ at lithium sites. The trapped electron centers become Ag^0 ($4d^{10}5s^1$) and the trapped hole centers, or recombination centers, become Ag^{2+} ($4d^9$). Evidence for these centers is seen in EPR at room temperature. Optical absorption of the irradiated crystal showed a broad peak near 370 nm. Bleaching with 400 nm light decreased the EPR signals of the Ag^0 and Ag^{2+} centers. When the crystal was stimulated with 400 nm light, OSL was produced with 270 nm emission. The effects of the stimulating light's flux on OSL were observed by using xenon lamp and diode laser sources. OSL, with the laser at 405 nm, decayed faster, and provided insight on the existence of a competing electron trap, oxygen vacancies.

15. SUBJECT TERMS
Luminescence, Optically Stimulated Luminescence, Lithium Tetraborate ($Li_2B_4O_7$), Silver-doped

16. SECURITY CLASSIFICATION OF:			**17. LIMITATION OF ABSTRACT**	**18. NUMBER OF PAGES**	**19a. NAME OF RESPONSIBLE PERSON**
					Maj Eric M. Golden
a. REPORT	**b. ABSTRACT**	**c. THIS PAGE**			**19b. TELEPHONE NUMBER** (Include Area Code)
U	U	U	UU	85	(937) 255-3636, x4518; eric.golden@afit.edu